AGU PUBLICATIONS

JGR

Journal of Geophysical Research: Oceans

RESEARCH ARTICLE

10.1002/2017JC013509

Key Points:
- Upper OMZ layer is mainly ventilated by mean circulation inside the Subtropical Cell (STC). Below the STC, turbulence dominates ventilation
- One-way dianeutral entrainment accounts for 25.8% of the oxygen lost in this OMZ, most of it upwelling into the Ekman layer within the STC
- The tropical-equatorial pathway provides 59.9% of the net oxygen supply while the subtropical pathway contributes with 28.6%

Supporting Information:
- Supporting Information S1

Correspondence to:
P. J. Llanillo,
pedro.llanillo@usach.cl

Citation:
Llanillo, P. J., Pelegrí, J. L., Talley, L. D., Peña-Izquierdo, J., & Cordero, R. R. (2018). Oxygen pathways and budget for the eastern South Pacific Oxygen Minimum Zone. *Journal of Geophysical Research: Oceans*, *123*, 1722–1744. https://doi.org/10.1002/2017JC013509

Received 28 SEP 2017
Accepted 28 JAN 2018
Published online 2 MAR 2018
Corrected 31 MAR 2018

This article was corrected on 31 MAR 2018. See the end of the full text for details.

Oxygen Pathways and Budget for the Eastern South Pacific Oxygen Minimum Zone

P. J. Llanillo[1], J. L. Pelegrí[2,3], L. D. Talley[4], J. Peña-Izquierdo[2], and R. R. Cordero[1]

[1]Universidad de Santiago de Chile, Santiago, Chile, [2]Departament d'Oceanografia Física i Tecnològica, Institut de Ciències del Mar, CSIC, Barcelona, Spain, [3]Laboratorio Internacional de Cambio Global (LINCGlobal), ICM-CSIC, Barcelona, Spain, [4]Scripps Institution of Oceanography, University of California San Diego, San Diego, California, USA

Abstract Ventilation of the eastern South Pacific Oxygen Minimum Zone (ESP-OMZ) is quantified using climatological Argo and dissolved oxygen data, combined with reanalysis wind stress data. We (1) estimate all oxygen fluxes (advection and turbulent diffusion) ventilating this OMZ, (2) quantify for the first time the oxygen contribution from the subtropical versus the traditionally studied tropical-equatorial pathway, and (3) derive a refined annual-mean oxygen budget for the ESP-OMZ. In the upper OMZ layer, net oxygen supply is dominated by tropical-equatorial advection, with more than one-third of this supply upwelling into the Ekman layer through previously unevaluated vertical advection, within the overturning component of the regional Subtropical Cell (STC). Below the STC, at the OMZ's core, advection is weak and turbulent diffusion (isoneutral and dianeutral) accounts for 89% of the net oxygen supply, most of it coming from the oxygen-rich subtropical gyre. In the deep OMZ layer, net oxygen supply occurs only through turbulent diffusion and is dominated by the tropical-equatorial pathway. Considering the entire OMZ, net oxygen supply (3.84 ± 0.42 μmol kg^{-1} yr^{-1}) is dominated by isoneutral turbulent diffusion (56.5%, split into 32.3% of tropical-equatorial origin and 24.2% of subtropical origin), followed by isoneutral advection (32.0%, split into 27.6% of tropical-equatorial origin and 4.4% of subtropical origin) and dianeutral diffusion (11.5%). One-quarter (25.8%) of the net oxygen input escapes through dianeutral advection (most of it upwelling) and, assuming steady state, biological consumption is responsible for most of the oxygen loss (74.2%).

Plain Language Summary Large oceanic volumes with very low dissolved oxygen concentrations are a natural feature of the world ocean. Their existence is explained as a combination of weak water renewal plus large biological oxygen consumption. These low-oxygen regions are expected to expand due to climate change, which will likely damage marine habitats and threaten the sustainability of important fisheries. Here we describe the mean state of the world's second most intense low-oxygen volume, located in the tropical eastern South Pacific. For this purpose, we consider and quantify the physical processes oxygenating this low-oxygen volume, including the contribution of vertical oxygen transport. We find that turbulence provides two-thirds of the overall oxygen supply whereas mean currents contribute with one-third. Regarding the pathway of origin, almost two-thirds of the total oxygen supply takes place from the tropical-equatorial region while a previously unaccounted subtropical pathway provides for about one-quarter of the oxygen. Remarkably, one-quarter of all the oxygen supplied to the low-oxygen volume escapes through vertical transport, most of it upwelling into the Ekman layer. This study provides a necessary comparative baseline for future studies of how climate change may disrupt the mean-state of this important low-oxygen oceanic volume.

1. Introduction

The eastern South Pacific (ESP) Oxygen Minimum Zone (OMZ) (Figures 1a and 1b) is a large oceanic volume characterized by low dissolved oxygen levels (Fiedler & Talley, 2006). The ESP-OMZ is found west of South America between about 35°S and the Equator, with its lowest oxygen values located along 7.5°S at depths of about 350 m ($\gamma_n = 26.81$ kg m^{-3}). The core oxygen values fall below 19.5 μmol kg^{-1} (Paulmier & Ruiz-Pino, 2009), and the oxygen concentration delimiting the ESP-OMZ is usually taken between 60 and 120 μmol kg^{-1},

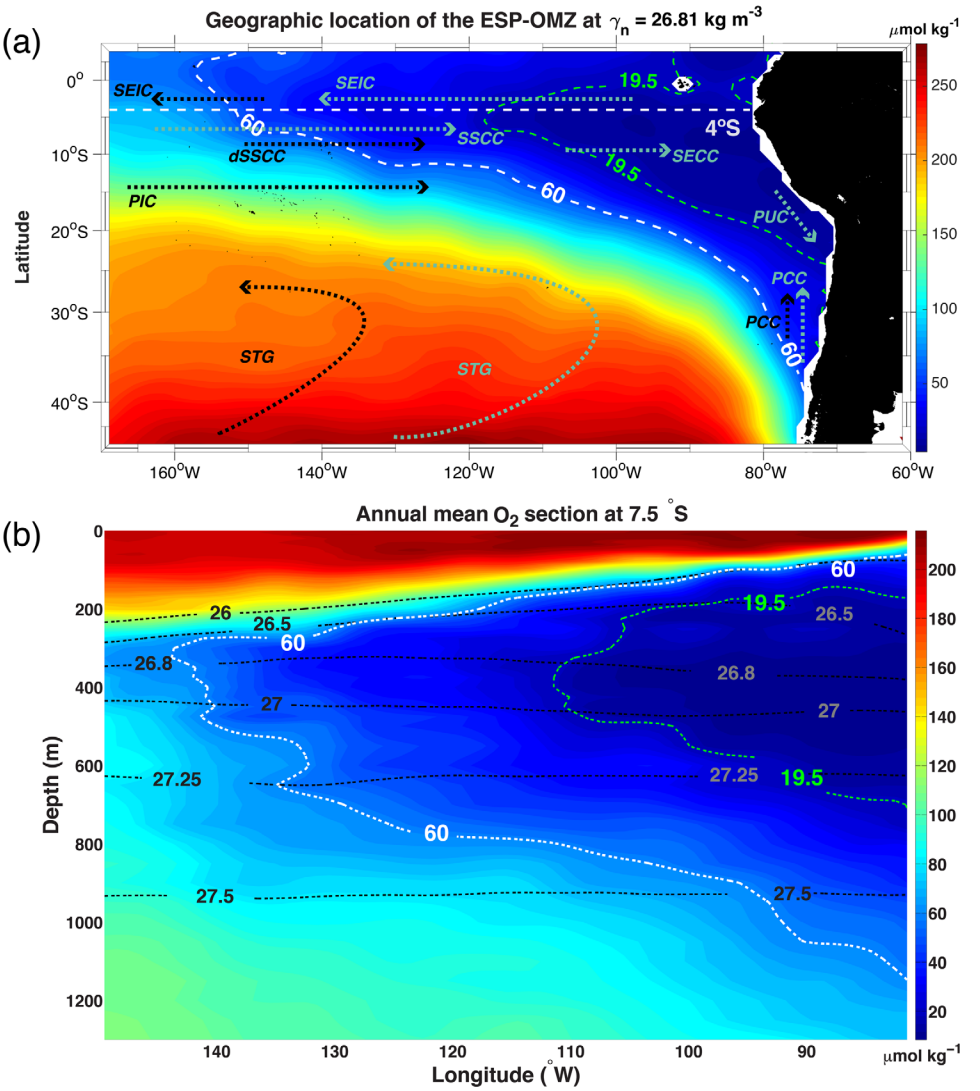

Figure 1. (a) Map of the study area with the ESP-OMZ delimited by the oxygen contour of 60 μmol kg^{-1} (white dashed line) and its core delimited by the oxygen contour of 19.5 μmol kg^{-1} (green dashed line). The background shows the climatological mean dissolved oxygen (μmol kg^{-1}) from WOA-13 at the neutral surface of the ESP-OMZ core (γ_n = 26.81 kg m^{-3}, $z \cong 350$ m). The principal currents discussed in the paper are sketched: near-surface currents are depicted in light green and intermediate currents in black. Currents: SSCC, Southern Subsurface Countercurrent; dSSCC, deep SSCC; PIC, Polynesian Intermediate Current; SECC, South Equatorial Countercurrent; SEIC, South Equatorial Intermediate Current; PUC, Poleward Undercurrent; STG, subtropical gyre flow; and PCC, Peru-Chile Current. (b) Vertical section of the climatological mean dissolved oxygen from WOA-13 at 7.5°S. Neutral density contours are included for reference (black dashed lines).

a range that is often assumed to represent conditions that affect many marine species (e.g., Stramma et al., 2010a); however, Hofmann et al. (2011) have shown that the oxygen partial pressure (pO_2) is a better indicative of the physiological state of marine life, with the 60 μmol kg^{-1} being equivalent to a pO_2 of about 48 matm at 12°C. The thickness of the ESP-OMZ decreases progressively westward (Figure 1b), with maximum values greater than 1,000 m close to the Peruvian coast when defining the boundary of the ESP-OMZ by the 60 μmol kg^{-1} oxygen isosurface. Here, despite their equatorial connection, we consider the ESP-OMZ as independent from the eastern North Pacific OMZ (Karstensen et al., 2008; Keeling et al., 2010).

The concentration of dissolved oxygen is decreasing in low-latitude oceans, with oxygen in the OMZs reaching thresholds that stress organisms (Czeschel et al., 2012, 2015; Helm et al., 2011; Schmidtko et al., 2017; Stramma et al., 2008, 2010b). The OMZs expansion will likely reduce the habitat and threaten the sustainability of important pelagic fisheries maintained by the high biological productivity overlying these areas (Strub et al., 1998),

and will further disrupt the carbon and nitrogen global cycles (Kalvelage et al., 2013). At the suboxic core (oxygen less than 19.5 μmol kg^{-1}) of the ESP-OMZ, nitrate (NO_3) replaces oxygen for respiration of organic matter (Oguz et al., 2000; Smethie, 1987). This process has important implications as the (oceanic-fixed) nitrogen reduced in the core is eventually lost to the atmosphere as a greenhouse gas (N_2O) (Ulloa & Pantoja, 2009); further, after denitrification, nitrate becomes a limiting nutrient for primary production, hence weakening the oceanic biological carbon pump (Codispoti et al., 2001; Kalvelage et al., 2011, 2013; Morales et al., 1999).

The global warming signature in ocean deoxygenation, related to changes in the rates of ventilation, remineralization and oxygen solubility, is emerging beyond the natural variability in the observations (Ito et al., 2017). Models predict a general decrease of dissolved oxygen in the ocean as a result of man-made global warming modulated by natural decadal variability (Deutsch et al., 2011; Matear & Hirst, 2003; Schmittner et al., 2008), though they are not capable yet of properly reproducing the changes observed in the OMZs (Stramma et al., 2012).

The existence of the ESP-OMZ is usually explained as a combination of a weak water mass renewal rate, characteristic of shadow zones in tropical eastern boundary regions (Luyten et al., 1983), plus a large subsurface biological consumption of oxygen, typical of the productive eastern boundary upwelling systems (Helly & Levin, 2004; Keeling et al., 2010; Paulmier et al., 2006). Although the mechanisms sustaining the ESP-OMZ are fairly well understood (Karstensen et al., 2008), the pathways and intensity of its advective and diffusive ventilation are not properly defined. Here for the first time, we investigate all the oxygen fluxes into and out of the ESP-OMZ together. We examine the oxygen pathways, discerning between (1) isoneutral (quasi-horizontal) advection, (2) dianeutral (quasi-vertical) advection, (3) isoneutral turbulent diffusion, and (4) dianeutral turbulent diffusion. Further, we build an oxygen budget that allows us to quantify the role of respiration as an oxygen sink.

Previous studies of ESP-OMZ ventilation have focused on the oxygen supply through the equatorial eastward zonal currents (Czeschel et al., 2011, 2015; Montes et al., 2014; Stramma et al., 2010a). Nevertheless, Peña-Izquierdo et al. (2015) have recently highlighted the importance of the subtropical pathway in the ventilation of the North Atlantic (NA) shadow zone, showing that half of the water mass input to the core layers of the NA-OMZ comes directly from the NA subtropical gyre. Given this result, the possibility of an analogous subtropical advective supply of oxygen into the ESP-OMZ deserves consideration. Using climatological data, our study indeed confirms the existence of such a subtropical South Pacific pathway and provides the first estimate of the associated oxygen input. Our analysis of both the climatological subtropical pathway and the dianeutral oxygen supply into the ESP-OMZ provides both an improved view of the advective and turbulent oxygen contributions and a refined annual-mean oxygen budget for the second most intense OMZ of the world oceans (Paulmier & Ruiz-Pino, 2009).

The paper is structured as follows. In sections 2 and 3, we present the data sources and the methodology. In section 4, we briefly discuss the mean currents, the water masses, and the upper-thermocline circulation found in the region of the ESP-OMZ. In section 5, we analyze oxygen transports due to specific mean currents, quantify the advective and diffusive oxygen supply into the ESP-OMZ, and derive the annual-mean oxygen budget for this OMZ. Finally, in section 6, we summarize the main findings and highlight their relevance.

2. Data

We use two different global climatologies: the World Ocean Atlas 2013 (WOA-13) for dissolved oxygen and the Roemmich-Gilson Argo climatology (R-G Argo) for salinity and temperature. The WOA-13 climatology (http://www.nodc.noaa.gov/OC5/woa13/) provides annual-mean fields at standard depth levels with a 1° resolution (Garcia et al., 2014). The R-G Argo climatology (http://sio-argo.ucsd.edu/RG_Climatology.html) includes annual-mean salinity and temperature values, also on a 1° grid, obtained using Argo data from 1 January 2004 to 31 December 2012 (http://www.argo.ucsd.edu, http://argo.jcommops.org). Annual-mean fields of salinity, in situ temperature, and pressure from the Argo climatology are converted into fields of absolute salinity (SA) and conservative temperature (CT) (McDougall & Barker, 2011), which are then interpolated to neutral density surfaces (Jackett & McDougall, 1997) covering most of the water column from the sea surface to the ocean bottom, from $\gamma_n = 24.250$ to 27.875 kg m^{-3}.

To account for surface layer Ekman transport above the ESP-OMZ, and hence transport divergence and Ekman pumping, we compute a climatology of sea-surface mean wind stress from the Era-Interim reanalysis (Dee et al., 2011) for the same period as the Argo data (section 3). In addition, we use vertical velocities from SODA 2.2.4 reanalysis (Carton & Giese, 2008) and oxygen float data (Czeschel et al., 2015) to compare with our results.

3. Methods

We define the ESP-OMZ volume as the water volume enclosed by the 60 μmol kg^{-1} oxygen isosurface in the South Pacific, closed to the north by a zonal boundary at 4°S where the average oxygen concentration is 37.46 μmol kg^{-1}. As we rely on geostrophic balance to calculate horizontal flow, the 4°S boundary avoids the equatorial band, where the Coriolis force is too small to justify geostrophic equilibrium (e.g., Castellanos et al., 2015).

The ESP-OMZ extends vertically from $\gamma_n = 25.875$ to 27.625 kg m^{-3}; inside this volume, the isoneutral surfaces are set at constant intervals of 0.125 kg m^{-3}. The vertical separation between isoneutral surfaces ranges from about 20 m at $\gamma_n = 26.000$ kg m^{-3} to about 200 m at $\gamma_n = 27.600$ kg m^{-3}. The ESP-OMZ is divided into three vertical strata according to the annual-mean oxygen vertical distribution within the ESP-OMZ volume: the upper layers, where the dissolved oxygen decreases rapidly with depth (isoneutrals 25.87–26.75 kg m^{-3} and depths 65–325 m); the core, where oxygen has relatively uniform minimum values (26.75–26.87 kg m^{-3} and 325–385 m); and the deep layers, where oxygen increases progressively with depth (26.87–27.62 kg m^{-3} and 385–1160 m) (Figure 3).

Oxygen evolution at a given location is described by the advection-diffusion equation:

$$\frac{\partial O_2}{\partial t} + u\frac{\partial O_2}{\partial x} + v\frac{\partial O_2}{\partial y} + w\frac{\partial O_2}{\partial z} = O_{2ext} - aOUR + \frac{\partial}{\partial x}\left(K_x\frac{\partial O_2}{\partial x}\right) + \frac{\partial}{\partial y}\left(K_y\frac{\partial O_2}{\partial y}\right) + \frac{\partial}{\partial z}\left(K_z\frac{\partial O_2}{\partial z}\right) \quad (1)$$

where the directions (x, y) and velocities (u, v) are the zonal and meridional directions along isoneutral surfaces and z is the vertical direction with velocity w, to all effects taken to be in the direction normal to the isoneutrals (dianeutral); O_{2ext} is an external source or sink (air-sea interface), and $aOUR$ is the apparent oxygen utilization due to biological processes (positive for utilization, negative for production). The turbulent diffusivities in the (x, y, z) directions are (K_x, K_y, K_z), where the coefficients vary due to the differing sources of turbulence in the isoneutral and dianeutral directions and because of the asymmetry between eddy length scales in the zonal and meridional directions at the low OMZ latitudes. We assume that the turbulent diffusivities are constant in the direction of the diffusivity, although we do also assume that the isoneutral diffusivities decay with depth.

We examine the oxygen budget integrated over a closed volume encompassing the OMZ, so we evaluate the fluxes, rather than the flux divergences (equation (1)). The isoneutral and dianeutral advective fluxes are (uO_2, vO_2, wO_2), and the isoneutral and dianeutral turbulent diffusive fluxes are $(-K_x\partial O_2/\partial x,\ -K_y\partial O_2/\partial y,\ -K_z\partial O_2/\partial z)$, i.e., proportional to the gradients of dissolved oxygen concentration (O_2) along/across the isoneutral surfaces, with the negative sign accounting for downgradient oxygen diffusion (Figure 2b). We assume steady state within the framework of the climatologies we are using, so the first term in equation (1) vanishes. We consider a volume that is separated from the sea surface and below the mixing layer so O_{2ext} vanishes. We calculate all advective and diffusive terms (net oxygen supply) explicitly and diagnose $aOUR$ as the residual (i.e., the oxygen consumption needed to close the oxygen budget when assuming steady state).

The methods for calculating isoneutral advective fluxes are given in section 3.1; isoneutral and dianeutral diffusive fluxes in section 3.2; dianeutral advective flux (entrainment) in section 3.3; and volume integrals for the closed mass and oxygen budgets in sections 3.4 and 3.5.

3.1. Isoneutral Advective Flux

We use the approximate isoneutral geostrophic stream function φ ($m^2\ s^{-2}$) to map water pathways along neutral density surfaces, following McDougall and Klocker (2010). The geostrophic velocity field is related to the horizontal gradient of this stream function, $f(u-u_r,\ v-v_r) = (-\partial\varphi/\partial y,\ \partial\varphi/\partial x)$, where f is the Coriolis parameter, (u, v) correspond to the geostrophic velocities in the (x, y) directions (positive eastward and northward), and (u_r, v_r) are the unknown reference velocities.

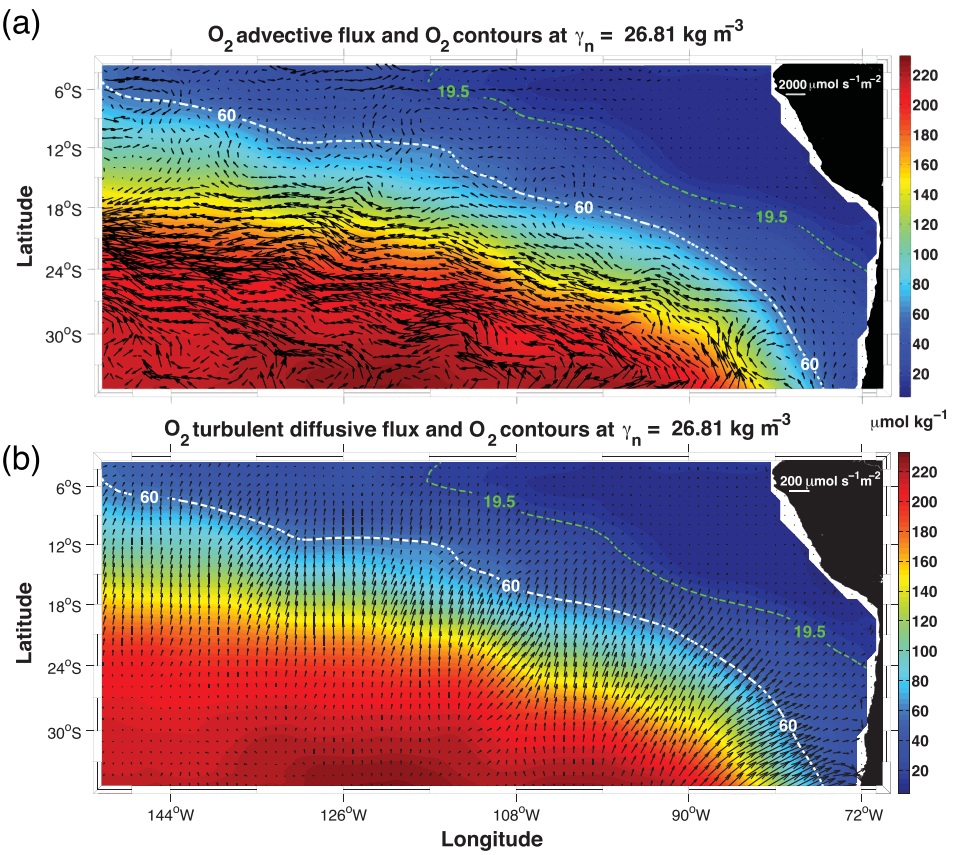

Figure 2. Distribution of isoneutral (a) advective and (b) turbulent oxygen fluxes (μmol s^{-1} m^{-2}) on the neutral surface γ_n = 26.81 kg m^{-3}. The ESP-OMZ boundary (contour of 60 μmol kg^{-1}) and its core (contour of 19.5 μmol kg^{-1}) are shown as dashed lines.

In order to constrain the geostrophic reference velocities, we search for a reference pressure level that best conserves mass within the ESP-OMZ volume. Specifically, we compute the divergence of the surface Ekman transports above the shallowest layer of the ESP-OMZ and the divergence of the geostrophic advective volume transports within the ESP-OMZ volume and within the volume bounded by the projection of the shallowest OMZ layer onto the Ekman layer; and select a single reference level that leads to the minimum total volume divergence. We find that volume is approximately conserved with a reference level of 1,100 dbar, which is in good agreement with Zilberman et al. (2013) who used a reference level of no motion at 1,000 dbar for a zonal section along 7.5°S in the Pacific. The divergence of the horizontal Ekman transports (1.51 Sv) in the surface Ekman layer (section 3.3) is partially compensated by the geostrophic transport convergence (−0.60 Sv) in this layer. The rest of the volume needed to conserve mass in the Ekman layer comes from convergence (−0.91 Sv) of isoneutral advection in the upper layers of the OMZ that upwells into the Ekman layer through dianeutral advection. Considering the entire OMZ volume, the net imbalance is −2.51 Sv, resulting from the geostrophic transport convergence (−3.42 Sv) and the 0.91 Sv upwelling into the Ekman layer (supporting information Figure S1).

We compute the annual-mean geostrophic oxygen flux (kmol s^{-1} m^{-2}) along selected isoneutrals as the product of the absolute geostrophic velocity (m s^{-1}) and the dissolved oxygen concentration (kmol m^{-3}). The isoneutral advective oxygen flux into and out of the ESP-OMZ is computed as the flux normal to the OMZ boundary. Figure 2a illustrates the annual-mean isoneutral advective oxygen flux on the isoneutral that cuts through the ESP-OMZ core (γ_n = 26.81 kg m^{-3}, $z \cong$ 350 m).

3.2. Isoneutral and Dianeutral Diffusive Fluxes

The diffusive fluxes reflect the existence of turbulence that exchanges water parcels with different oxygen concentrations, with the dissimilar diffusivities due to the differing origin of turbulence in the three

Cartesian directions. Turbulence is associated with no net water volume exchange, but rather produces a nonzero net flux of oxygen in the direction from highest to smallest concentrations. This is the standard downgradient diffusion.

The annual-mean dissolved oxygen data from WOA-13, interpolated on neutral surfaces, are used to compute the isoneutral and dianeutral oxygen gradients in the ESP-OMZ. For the isoneutral eddy diffusivities, we use the zonal ($K_x \cong 4.8 \times 10^3$ m^2 s^{-1}) and meridional ($K_y \cong 2.3 \times 10^3$ m^2 s^{-1}) sea surface values from Chaigneau and Pizarro (2005), obtained from reinitialized surface drifter trajectories in the region covering the ESP-OMZ. According to Hahn et al. (2014), the eddy diffusivity decreases by 78% in the depth interval from 100 to 1,000 m in the North Atlantic OMZ (NA-OMZ). Due to the lack of similar studies for the ESP-OMZ, we fit an exponentially decreasing function to the isoneutral eddy diffusivities, imposing the same 78% decrease at 1,000 m relative to the sea surface. The dianeutral eddy diffusion coefficient (K_z) is set to a constant 10^{-5} m^2 s^{-1}, as estimated by Fischer et al. (2013) for the NA-OMZ and within the range of values inferred by Whalen et al. (2012) using Argo data from the ESP.

3.3. Ekman Pumping and Dianeutral Advection

The ESP-OMZ is located immediately below the base of the annual-mean surface mixed layer (supporting information Figure S2). Hence, the ESP-OMZ is affected by the divergence of the wind-induced Ekman transport above the OMZ, in a surface region defined as the vertical projection of the uppermost ESP-OMZ density layer. Using sea-surface mean wind stress data from the ERA-Interim reanalysis, we compute this Ekman transport divergence (upwelling) to be 1.51 Sv.

We vertically discretize the ESP-OMZ volume as a series of size-varying superimposed slabs with vertical walls and upper and lower boundaries along isoneutral surfaces. The shape of each slab is defined by the 60 μmol kg^{-1} oxygen contour on its central isoneutral surface. We start with the shallowest OMZ slab, where the vertical volume transport through its upper boundary (0.91 Sv of Ekman suction) is set by the combination of sea-surface Ekman transport divergence (1.51 Sv) and geostrophic transport convergence (−0.60 Sv). In this first slab there is a small convergence of the isoneutral advective flux (−0.08 Sv) (supporting information Figure S1). Balancing the net volume transport in this slab provides the required dianeutral advection (entrainment) between this level and the underlying one. Applying the same procedure to all layers, down to the deepest slab of the ESP-OMZ, leads to the dianeutral transports between all adjacent slabs required to conserve mass in each slab (supporting information Figure S1). Notice that, because of the different sizes of the superimposed slabs, volume (and oxygen) can also enter or leave the ESP-OMZ through dianeutral advection in each slab. Since the ESP-OMZ is completely confined, the dianeutral water divergence out of the entire control volume (including the water lost through upwelling into the Ekman layer) exactly compensates for the isoneutral volume convergence (−3.42 Sv).

The dianeutral (quasi-vertical) velocities (w) at the top and base surfaces of each slab are hence obtained dividing the dianeutral transports by the corresponding areas. These dianeutral velocities can be compared with two independent estimates (Figure 3). The first one comes from a similar procedure but starting the calculations at the deepest layer, imposing zero dianeutral velocity at the base of the OMZ. The second estimate is the average dianeutral velocity from the SODA 2.2.4 reanalysis for each of the ESP-OMZ layers. All w vertical profiles are very similar, lending good confidence to the results.

It is worth emphasizing the difference between dianeutral diffusion (section 3.2) and the above dianeutral advection (entrainment). Dianeutral diffusion is the outcome of vertical instabilities leading to two-way water exchange across the isoneutrals, i.e., taking place simultaneously in opposite vertical directions. This is the classical diffusive perspective with zero net mass exchange but with nonzero property transfer occurring in the downgradient direction; in box models, this exchange has sometimes been named two-way exchange (Pelegrí & Csanady, 1991). In contrast, we may imagine a situation with a stationary mean state (annual-mean isoneutral surfaces) that, nevertheless, experiences a net water transfer in one vertical direction. In this mean reference frame, this dianeutral transfer represents a diffusive flux with a net mass transfer resulting from processes such as intermittent entrainment (Turner, 1986) or the correlation of layer thickness and velocity (Csanady, 1989). However, in order to emphasize the difference with the previous two-way diffusive process, we will call it dianeutral advection/velocity/flow (or simply entrainment); in box models, it has been named entrainment or one-way transfer (Pelegrí & Csanady, 1991).

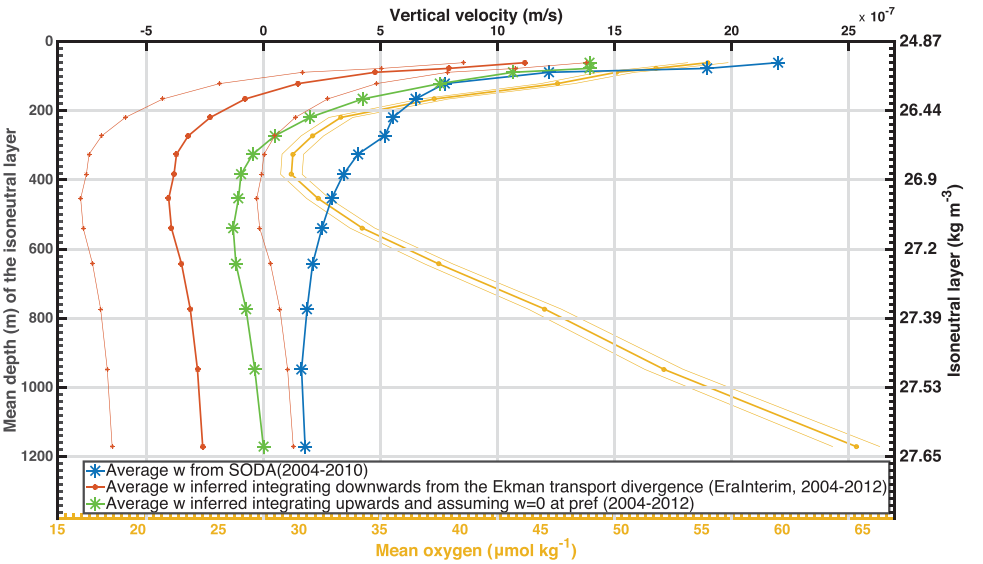

Figure 3. Vertical profiles of the dianeutral velocity w (m s^{-1}) obtained imposing volume conservation inside the ESP-OMZ: (1) with w set at the base of the sea-surface mixed layer from the divergence of the wind-induced Ekman transport (red line) and (2) imposing zero w at the base of the ESP-OMZ (green line); (3) w is also calculated as the average ESP-OMZ value from SODA 2.2.4 reanalysis data (blue line). The thin red lines represent the 95% confidence interval for our estimation of w, computed from the error in Ekman transport divergence. The vertical profile of the mean oxygen concentration (μmol kg^{-1}, yellow line) corresponds to the lids the isoneutral slabs used to discretize the ESP-OMZ. The shallowest point of each curve is located at the base of the annual-mean sea-surface mixed layer.

In the ESP-OMZ, the dianeutral velocities respond to the combined effect of Ekman divergence (upwelling) in the surface mixed layer and geostrophic divergence within each layer. These dianeutral fluxes induce a net transfer of water and whatever substance is dissolved in the water (such as oxygen) between layers. The observed pattern of the divergence of the dianeutral advection (change of w with depth, Figure 3) is consistent with the idea that the OMZ core is a region of minimum turbulence (i.e., with minimum divergence of the dianeutral advection and, thus, with minimum entrainment between the OMZ core layer and the neighboring layers). This contrasts with the larger divergence/convergence of the dianeutral advective flux above/below the OMZ core and neighboring layers, which suggests more turbulent layers (better ventilated). In a simple downgradient diffusive-flux parameterization we could parameterize such a process by setting a depth-variable vertical diffusion coefficient K_z (Pelegrí & Csanady, 1994); given the difficulty of choosing a proper K_z depth dependence, we rather set a constant value and calculate the dianeutral velocities (entrainment) that satisfy mass conservation for each layer.

3.4. Net Volume and Oxygen Transports

The isoneutral advective volume transport (in Sv, 1 Sv = 10^6 m^3 s^{-1}) and oxygen transport (kmol s^{-1}) across the surface delimiting the ESP-OMZ are the integral of the geostrophic velocities and oxygen fluxes across the lateral vertical elements of area. These are calculated as a discrete representation of the following integrals:

$$\oint_C \vec{v} \cdot \overrightarrow{dS} = \oint_C v_\perp \frac{\partial z}{\partial n}\, dn\, ds; \qquad \oint_C \rho O_2 \vec{v} \cdot \overrightarrow{dS} = \oint_C \rho O_2 v_\perp \frac{\partial z}{\partial n} dn\, ds \tag{2}$$

where $\vec{v}$ is the (geostrophic) velocity (m s^{-1}), ρ is density (kg m^{-3}) and the O_2 (μmol kg^{-1}) is taken along the ESP-OMZ boundary (O_2 is 60 μmol kg^{-1} except along the zonal northern boundary at 4°S), z is the vertical coordinate between isoneutral surfaces, s is the horizontal coordinate along those contours C delimiting the ESP-OMZ, $\overrightarrow{dS}$ is the horizontal vector normal to a vertical element of area along the contour C, with size $(dz\ ds)$, and $v_\perp$ is the component of the velocity normal to the element of vertical area. In practice, the element of vertical area is specified in isoneutral coordinates, with the vertical distance δz between two isoneutral surfaces separated by a neutral density increment $\delta n = 0.125$ kg m^{-3} given by $\delta z = \delta n\ (\partial z/\partial n)$.

Hence, a discrete element of area is $\delta S = \delta s\ \delta z = \delta s\ \delta n\ (\partial z/\partial n)$, where δs represents a discrete element of horizontal distance along contours surrounding the volume of integration.

Similarly, the isoneutral diffusive transport of oxygen into the closed OMZ volume is calculated as the discrete form of the following expression:

$$\oint_C \rho\left(K_x \frac{\partial O_2}{\partial x}\hat{i} + K_y \frac{\partial O_2}{\partial y}\hat{j}\right) \cdot \overrightarrow{dS} = \oint_C \rho\left(K_x \frac{\partial O_2}{\partial x}dy + K_y \frac{\partial O_2}{\partial y}dx\right) \frac{\partial z}{\partial n}dn \tag{3}$$

where $\hat{i}$ and $\hat{j}$ represent the unit vectors in the (x, y) directions.

The dianeutral advective and diffusive fluxes are integrated across the upper and lower surfaces of each individual isoneutral layer comprising the ESP-OMZ, with horizontal area A. The dianeutral advective volume and oxygen transports are given by

$$\oint_A \vec{w} \cdot \overrightarrow{dA} = \oint_A w\ dxdy; \qquad \oint_A \rho\overline{O_2}\vec{w} \cdot \overrightarrow{dA} = \oint_A \rho\overline{O_2} w\ dxdy \tag{4}$$

where $\overrightarrow{dA}$ is the vertical vector normal to a horizontal element of area along the isoneutral, with size $(dx\ dy)$, and $\overline{O_2}$ (μmol kg^{-1}) is the average oxygen concentration in the area crossed by the dianeutral velocity w. The dianeutral diffusive oxygen transport is given by

$$\oint_A K_z \rho \frac{\partial O_2}{\partial z}\ \hat{k} \cdot \overrightarrow{dA} = \oint_A K_z \rho \frac{\partial O_2}{\partial z}\ dxdy \tag{5}$$

where $\hat{k}$ is the unit vector in the vertical direction.

3.5. Closing the Oxygen Budget

We calculate the divergence of the (isoneutral and dianeutral) advective and diffusive oxygen transports in the ESP-OMZ by integrating the oxygen fluxes across its entire closed boundary. Recall the advective water mass transport is balanced across the OMZ boundary but the advective oxygen transport is not. Combining the sources and sinks of oxygen, and ignoring the relatively minor density changes, the annual-mean oxygen budget for each layer and the entire volume is:

$$0 = \oint_C O_2\vec{v} \cdot \overrightarrow{dS} + \oint_A \overline{O_2}\vec{w} \cdot \overrightarrow{dA} - \oint_C \left(K_x \frac{\partial O_2}{\partial x}\hat{i} + K_y \frac{\partial O_2}{\partial y}\hat{j}\right) \cdot \overrightarrow{dS} - \oint_A K_z \frac{\partial O_2}{\partial z}\hat{k} \cdot \overrightarrow{dA} + \iiint_V aOUR \cdot dV \tag{6}$$

Therefore, the apparent oxygen utilization *aOUR* through biological processes (with units of oxygen concentration per unit time, positive for utilization, negative for production) can be determined from the imbalances in advective and diffusive oxygen transports within the ESP-OMZ.

Alternatively, Karstensen et al. (2008) assessed the *aOUR* in the Pacific OMZs through the combination of utilization estimates and water mass ages as derived from the CFC-11/^{14}C ratio, both provided in the GLODAP data set (Sabine et al., 2005). They adjusted their data (in μmol kg^{-1} yr^{-1}) to an exponential decay with depth, for the depth range from 100 to 1,500 m:

$$aOUR(z) = -0.5 + 12.0e^{-0.0021z} \tag{7}$$

After integration, this expression provides the mean rate of biological consumption of oxygen, either within each isoneutral layer or for the entire ESP-OMZ. The oxygen consumption for the top 300 m is slightly higher than in other regions of the North Pacific (Keeling et al., 2010), probably reflecting the high surface biological productivity above this OMZ. Most of the oxygen consumption in the ESP-OMZ is due to pelagic respiration so we assume that benthic respiration in the sediments is negligible (Brandt et al., 2015).

Recent observational works (Ito et al., 2017; Schmidtko et al., 2017) indicate widespread oxygen decline in the global ocean, but show very weak trends for the ESP-OMZ area, where oxygen concentrations are already very low. For the purpose of this study, we can reasonably assume that there is no net oxygen trend and that the ESP-OMZ is in steady state (i.e., the volume integral of the local rate of change in equation (6) is zero). Then, equations (6) and (7) provide independent estimates of the volume-averaged *aOUR*.

3.6. Error Propagation Analysis

We require error estimates for all variables and parameters in order to assess the error associated with the oxygen transports and the integrated rate of oxygen change. Chaigneau and Pizarro (2005) estimated the zonal and meridional eddy diffusivity errors to be $\pm 0.3 \times 10^3$ and $\pm 0.2 \times 10^3$ m^2 s^{-1}, respectively, for a 95% confidence interval. Fischer et al. (2013) estimated the vertical turbulent diffusivity error to be $\pm 0.2 \times 10^{-5}$ m^2 s^{-1}, for a 95% confidence interval.

Karstensen et al. (2008) estimated a 40% error, for a 95% confidence interval, in the expression for *aOUR* (equation (7)). In addition, oxygen concentration standard errors are provided in WOA-13; after averaging over the entire study region, the resulting value ($\pm 2.32 \times 10^{-6}$ kmol m^{-3}) is multiplied by 1.96 (assuming a Gaussian distribution) to obtain the oxygen concentration error with a 95% confidence interval: $\pm 4.54 \times 10^{-6}$ kmol m^{-3}.

Finally, our estimate for the average error in the isoneutral advective velocity is ± 0.16 cm s^{-1} while for the dianeutral advective velocity is $\pm 3.61 \times 10^{-5}$ cm s^{-1}, both at the 95% confidence interval (more details in supporting information).

Given all these individual errors, the accumulated errors for all advective and diffusive terms in the oxygen budget (equation (6)) are obtained from the individual errors, with a 95% confidence interval, through a standard propagation error technique, as described in supporting information.

4. Circulation and Water Masses in the ESP-OMZ

To describe the mean flow, we use a combination of geopotential, geostrophic velocity, and potential vorticity fields together with volume-transport Eulerian stream functions. To distinguish between the tropical-equatorial and subtropical pathways, we consider that the subtropical gyre and the equatorial system of currents are separated by a region with minimum geopotential anomaly values (Figure 4), and look for the point where this axis intersects with the boundary of the ESP-OMZ. The flow entering the ESP-OMZ south of this location is considered to belong to the subtropical pathway while flow entering north of this point is associated with the tropical-equatorial pathway. The point dividing the two pathways is located in a latitude range between 9°S and 20°S, with this latitude increasing with neutral density. Note that the currents of the tropical-equatorial route are predominantly zonal whereas the currents associated with the subtropical route have a leading meridional component.

The different pathways of the geostrophic flow can also be inferred from analysis of the volume-transport Eulerian stream function within a specific isoneutral layer (see supporting information for details on its computation). For instance, the stream function in the neutral density layer (thickness of 0.125 kg m^{-3}) that contains the ESP-OMZ core (centered at $\gamma_n = 26.81$ kg m^{-3}, $z \cong 350$ m in the ESP-OMZ region) shows the presence of both along-slope (east of 81°W) and interior-gyre currents belonging to the subtropical pathway (supporting information Figure S4a). The influence of waters from tropical-equatorial origin (flowing eastward or southeastward) is clear in the northern domain, with a dominant zonal component that creates a cyclonic gyre entering the ESP-OMZ northwest of (12°S, 117°W) and exiting between this latitude and about (18°S, 99°W). South of this last coordinate, the flow in this layer is dominated by the subtropical anticyclonic gyre.

4.1. Mean Currents

The tropical-equatorial advective pathway into the ESP-OMZ is composed of eastward geostrophic currents plus the flow entering the OMZ across its northern boundary at 4°S. Figure 4a shows a zonal eastward current between 4°S and 6°S centered at $\gamma_n = 26.56$ kg m^{-3} ($z \cong 247$ m), which we identify with the South Pacific Tsuchiya Jet (Tsuchiya, 1975), also known as the southern Subsurface Countercurrent (SSCC) (Kessler, 2006; Stramma et al., 2010a). Rowe et al. (2000) found the SSCC core at $\gamma_n = 26.5$ kg m^{-3} (Figure 5a, its corresponding oxygen flux is shown in supporting information Figure S5a), with this neutral surface rising eastward from 240 m at 126°W to 150 m at 110°W; these authors also identified a secondary SSCC (sSSCC) at 8°S that does not show up in our results (see also Stramma et al., 2010a). Below the SSCC core, we still detect a coherent but weaker eastward flow down to $\gamma_n = 27.47$ kg m^{-3} ($z \cong 900$ m). We refer to this flow as the deep SSCC (dSSCC) (Figure 5a).

There is a large-scale zonal low of geopotential anomaly between about 12°S and 20°S, shown at 27.19 kg m^{-3} ($z \cong 590$ m) in Figure 4c. This feature was previously identified by Tsuchiya and Talley (1996) as a trough in all

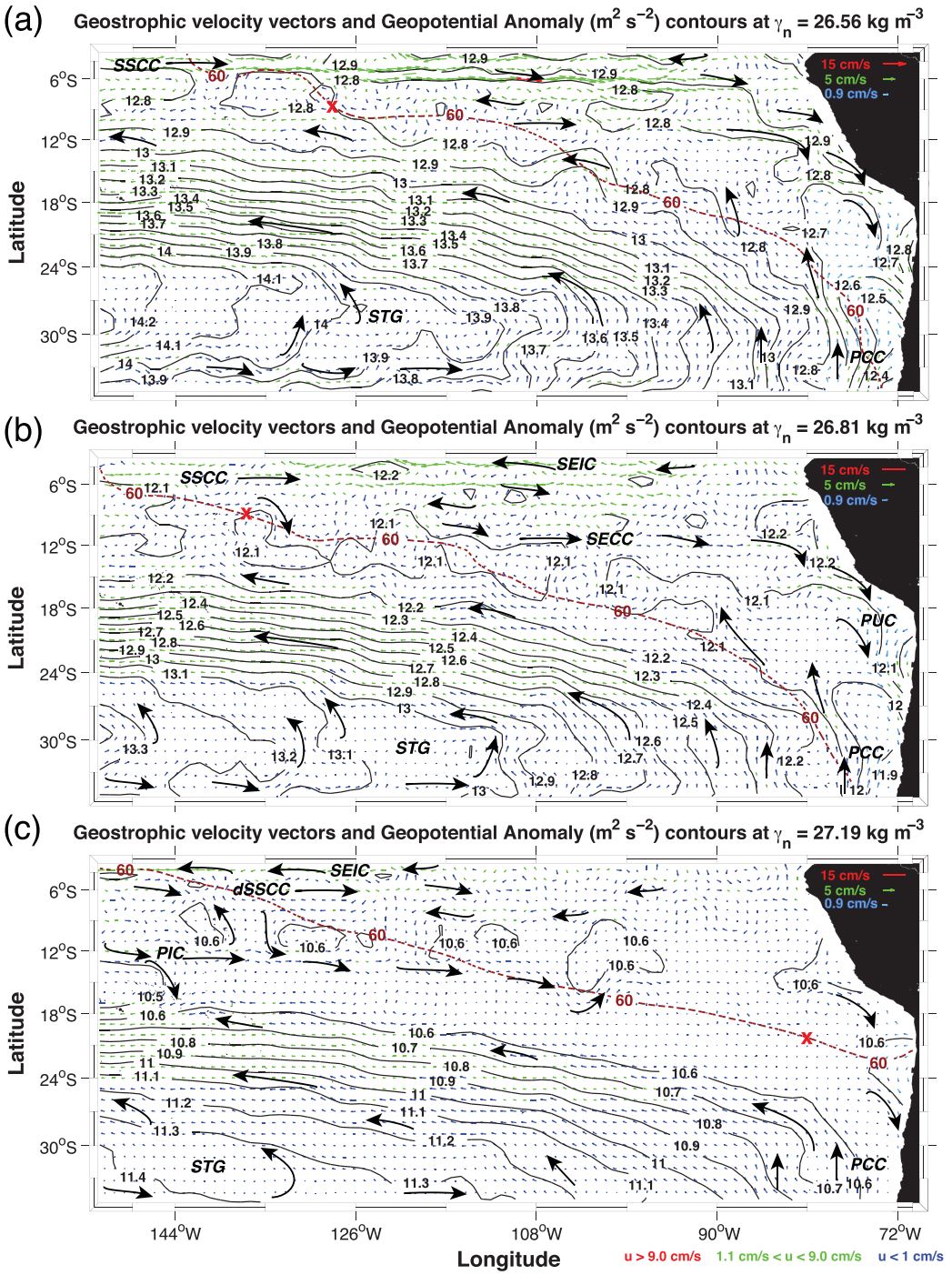

Figure 4. Geostrophic velocity vectors (cm s^{-1}) and geopotential anomaly contours (m^2 s^{-2}) on selected isoneutrals at: (a) γ_n = 26.56 kg m^{-3} ($z \cong 247$ m), (b) γ_n = 26.81 kg m^{-3} ($z \cong 350$ m), and (c) γ_n = 27.19 kg m^{-3} ($z \cong 590$ m). Currents: Southern Subsurface Countercurrent (SSCC), deep SSCC (dSSCC), Polynesian Intermediate Current (PIC), South Equatorial Countercurrent (SECC), South Equatorial Intermediate Current (SEIC), Poleward Undercurrent (PUC), subtropical gyre flow (STG), and Peru-Chile Current (PCC). The ESP-OMZ boundary (dissolved oxygen contour of 60 μmol kg^{-1}) is represented by a red dashed line. The red crosses indicates the latitudinal limit separating the tropical/equatorial and subtropical pathways at each layer.

isopycnals between 27.00 and 27.375 kg m^{-3}, centered at 12.5°S on WOCE's P17 section (along 135°W). Tsuchiya and Talley (1996) suggested that this feature causes an eastward geostrophic flow at 14°S that brings low inorganic nutrients and high oxygen, with oxygen decreasing toward the east consistent with

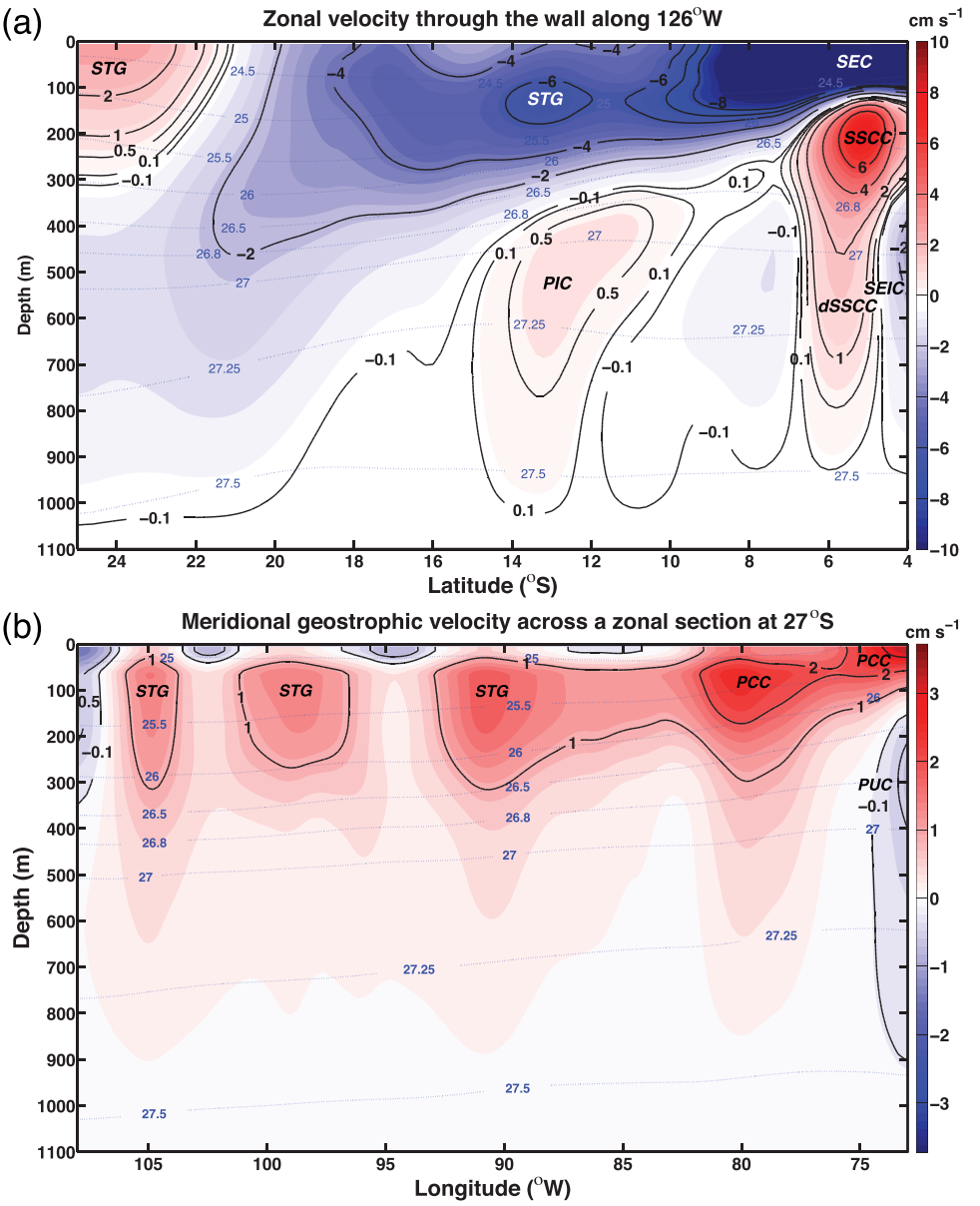

Figure 5. (a) Zonal geostrophic velocity (cm s^{-1}) across a meridional section at 126°W (positive eastward). (b) Meridional geostrophic velocity (cm s^{-1}) across a zonal section at 27°S (positive northward). The corresponding advective oxygen fluxes (mmol s^{-1} m^{-2}) are shown in supporting information Figures S5a and S5b. The Peru-Chile Current (PCC), the subtropical gyre meridional flow (STG), the Poleward Undercurrent (PUC), the southern Subsurface Countercurrent (SSCC), the deep SSCC (dSSCC), the South Equatorial Current (SEC), the South Equatorial Intermediate Current (SEIC), the Polynesian Intermediate Current (PIC), and the relevant neutral surfaces (blue dotted lines) are shown.

eastward flow. The signature of this eastward flow is also apparent at 14°S in WOCE's P16 and P18 sections, located on both sides of P17 (Talley, 2007). According to Reid (1997), the poleward displacement of the center of the subtropical gyre with depth enables this eastward flow to develop. In a modeling study, Nakano and Suginohara (2002) suggested that this flow would correspond to an arrested equatorial Rossby wave driven by equatorial winds. Our analysis is based on climatological fields, so the zonal persistence of this isopycnal trough indicates that the eastward flow is a general circulation feature.

For the sake of clarity, we henceforth refer to the eastward current between 12°S and 15°S, centered at 27.19 kg m^{-3}, as the Polynesian Intermediate Current (PIC) (Figures 4c and 5a, and supporting information Figure S5a). The PIC should not be confused with the shallower ($\gamma_n \leq$ 26.81 kg m^{-3}) and lower latitude

(10°S–12°S) South Equatorial Countercurrent (SECC) (Czeschel et al., 2011; Reid, 1959), which is found here between 117°W and 80°W (Figure 4b), well inside the ESP-OMZ boundary. Even though the PIC flows into the ESP-OMZ (Figure 4c), it has not previously been identified as an OMZ oxygen source. Similar subsurface zonal jets have recently been described in the North Pacific (Qiu et al., 2013) and in the tropical NA (Peña-Izquierdo et al., 2015), in the latter case along 14°N contributing to the ventilation of the less intense NA-OMZ with oxygen-rich subtropical waters.

The flow entering the ESP-OMZ through the boundary at 4°S is assumed to leak from the equatorial region north of 4°S. In this region, there is a set of alternating zonal currents, the eastward currents being richer in dissolved oxygen than the westward currents (Stramma et al., 2010a). The relevant eastward currents found between 4°S and the equator include the Equatorial Undercurrent (EUC) and the deeper (and weaker) but oxygen-richer South Intermediate Countercurrent (SICC) (Montes et al., 2010, 2014; Stramma et al., 2010a). Near the ESP-OMZ northern boundary, between the eastward dSSCC and SICC, we capture the signature of the westward South Equatorial Intermediate Current (SEIC) (Figure 5a) (Czeschel et al., 2011; Stramma et al., 2010a). Our results indicate a net climatological gain of volume (0.34 Sv) by mean currents across the ESP-OMZ boundary at 4°S, due to a volume gain (0.76 Sv) above $\gamma_n = 26.87$ kg m^{-3} that exceeds the volume loss (−0.42 Sv) below this isoneutral. Therefore, the upper layers present a leakage from the equatorial current system into the ESP-OMZ whereas the volume loss in the lower layers suggests that the SEIC is fed in part by the dSSCC, in good agreement with synoptic velocity studies (Czeschel et al., 2011; Stramma et al., 2010a).

We turn now to the mean currents belonging to the subtropical pathway. We distinguish two northward flows: the eastern-boundary Peru-Chile Current (PCC), also known as the Humboldt Current, and an interior flow along the northeastern part of the subtropical gyre (STG) and leaking into the OMZ (Table 1 and Figures 4a, 4b, and 5b, and supporting information Figure S5b). We consider these flows separately because of their different dynamical origins (e.g., Talley et al., 2011). At 30°S, the flow of the subtropical gyre can be separated from the PCC by the changing zonal gradient in geopotential anomaly, which is largest east of

Table 1
Volume (Sv) and Oxygen Transported (kmol s^{-1}) into the ESP-OMZ by Relevant Mean Currents, Specifying Their Vertical Range and Pathway of Origin (TE, Tropical-Equatorial and ST, Subtropical)

Currents range	Pathway	Current	Volume transport (Sv)	O_2 transport (kmol s^{-1})	% of O_2 transport	
Upper currents γ_n = 25.87 - 26.75 kg m^{-3} z = 65 - 325 m	TE	SSCC	1.931	118.1 ± 9.2	25.2 ± 2.0	77.5 ± 6.0
		4S_Eq	6.924	253.8 ± 19.7	54.1 ± 4.2	
		Others	1.558	97.2 ± 7.5	20.7 ± 1.6	
	ST	STG	1.168	63.6 ± 4.9	46.8 ± 3.6	22.5 ± 1.7
		PCC	0.633	72.4 ± 5.6	53.2 ± 4.1	
Currents at the core γ_n = 26.75 - 26.87 kg m^{-3} z = 325 - 385 m	TE	SSCC	0.061	3.8 ± 0.3	8.7 ± 0.7	58.9 ± 4.6
		4S_Eq	1.209	29.7 ± 2.3	67.8 ± 5.2	
		Others	1.437	10.3 ± 0.8	23.5 ± 1.8	
	ST	STG	0.347	21.1 ± 1.6	68.8 ± 5.3	41.1 ± 3.2
		PCC	0.174	9.5 ± 0.7	31.2 ± 2.4	
Deep currents γ_n = 26.87 - 27.50 kg m^{-3} z = 385 - 945 m	TE	PIC	1.401	86.4 ± 6.7	19.8 ± 1.5	94.0 ± 7.3
		dSSCC	3.610	153.3 ± 11.9	35.2 ± 2.7	
		4S_Eq (SEIC)	2.930	122.0 ± 9.5	28.0 ± 2.2	
		Others	1.229	74.0 ± 5.7	17.0 ± 1.3	
	ST	STG	0.302	18.1 ± 1.4	63.5 ± 4.9	6.0 ± 0.5
		PCC	0.164	9.7 ± 0.8	34.1 ± 2.6	

Note. The errors are estimated for a 95% confidence interval. Currents: SSCC, Southern Subsurface Countercurrent; dSSCC, deep SSCC; PIC, Polynesian Intermediate Current; 4S_Eq, flow entering through the boundary at 4°S, as the South Equatorial Intermediate Current (SEIC); STG, Subtropical Gyre flow; and PCC, Peru-Chile Current.

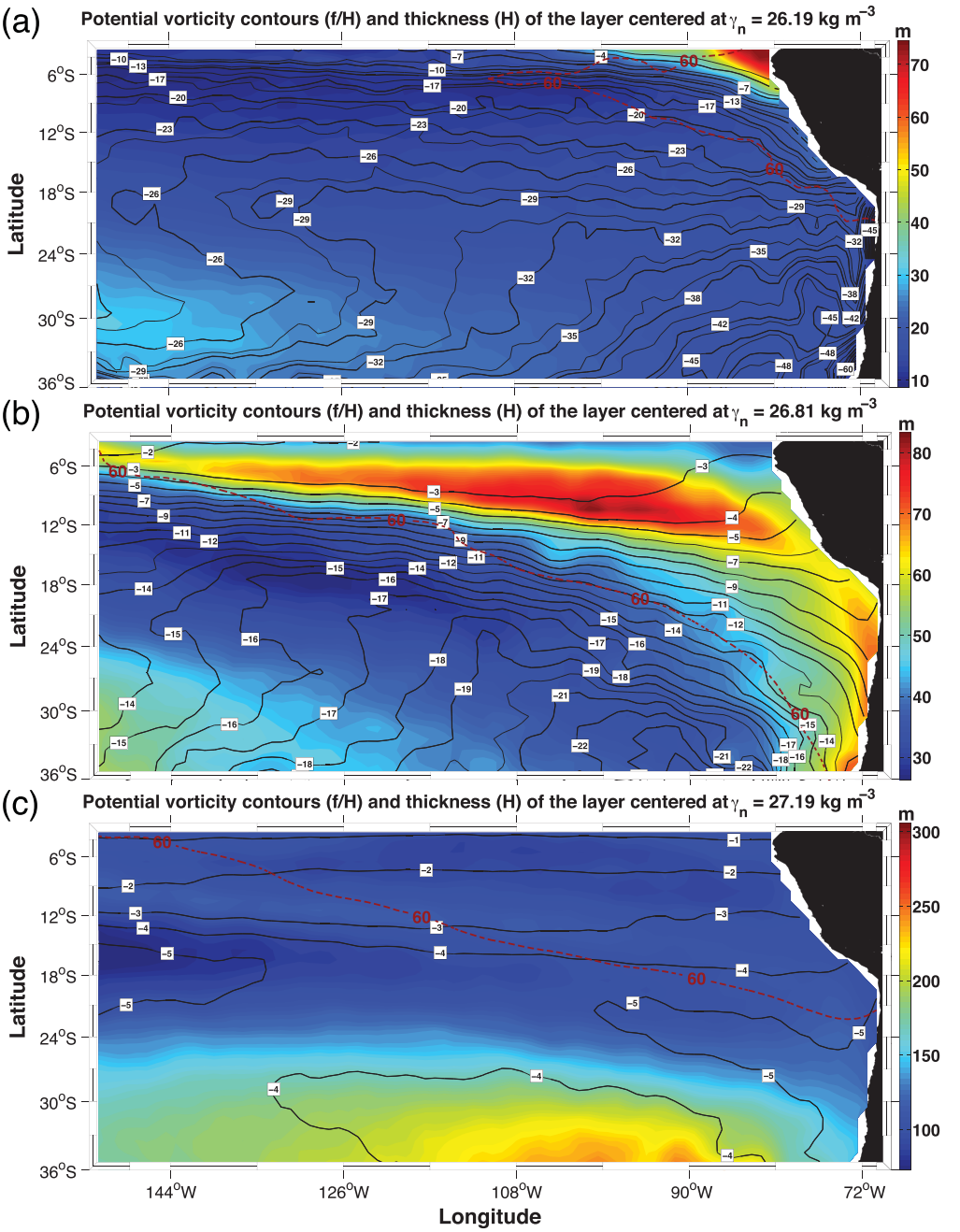

Figure 6. Potential vorticity contours ($\times 10^{-7}$ m^{-1} s^{-1}) computed for the isoneutral layers centered at (a) γ_n = 26.19 kg m^{-3}, (b) γ_n = 26.81 kg m^{-3}, and (c) γ_n = 27.19 kg m^{-3}. The background colors represent the thickness *H* of the isoneutral layer (m), all layers depicted are 0.125 kg m^{-3} thick. The ESP-OMZ boundary (dissolved oxygen contour of 60 μmol kg^{-1}) is represented by a red dashed line. The potential vorticity is calculated as *f*/*H*, where *f* is the Coriolis parameter; the geostrophic flow should follow the contours of *f*/*H*.

81°W (Figure 4a). The STG supply is enabled by the equatorward displacement of the tightly packed potential vorticity contours at isoneutral layers shallower than γ_n = 27.00 kg m^{-3} (Figures 6a and 6b). Flowing southward adjacent to the continental slope and centered at 300 m, we find the Poleward Undercurrent (PUC) (Gunther, 1936; Wooster & Gilmartin, 1961) (Figures 4a, 4b, and 5b, and supporting information Figure S5b). The PUC signature appears as a poleward deflection of the potential vorticity contours close to the South American coast (Figure 6b). This current is not involved in the ventilation of the ESP-OMZ as it develops within the OMZ volume.

The mean volume and oxygen transports by each current and pathway into the ESP-OMZ are detailed in section 5.1 (Table 1). The currents belonging to the tropical-equatorial pathway transport more volume into the ESP-OMZ than the subtropical currents at all levels, though the subtropical input is never negligible.

4.2. Water Masses and Upper-Thermocline Circulation

The water masses found in the eastern tropical South Pacific are the Subtropical Water (STW), Subantarctic Water (SAAW), Equatorial Subsurface Water (ESSW), Antarctic Intermediate Water (AAIW), and Pacific Deep Water (PDW) (Llanillo et al., 2013; Silva et al., 2009; Tsuchiya & Talley, 1998). The surface layer is dominated by STW. Below the mixed layer we find ESSW, representative of the ESP-OMZ and spreading between 100 and 600 m. The lower part of the ESSW partially mixes with the fresher and more oxygenated AAIW (centered at 700 m), while the upper part of the ESSW is partially ventilated by SAAW (centered at 150 m), resulting in a shallow salinity minimum (Karstensen, 2004; Reid, 1973; Tsuchiya & Talley, 1998). Below 1,200 m, PDW is the dominant water mass.

The southeasterly winds in the eastern tropical South Pacific induce the upwelling of nutrient-rich OMZ waters from the upper 160 m ($\gamma_n \leq$ 26.4 kg m^{-3}) (supporting information Figure S3 and Figure 3). These waters in turn sustain high surface primary production with intense subsurface organic matter remineralization and oxygen consumption (Fuenzalida et al., 2009). These upper layers appear embedded inside a 3-D circulation scheme where eastward flowing subsurface waters (SSCC) connect with subsurface poleward flow (PUC) (Montes et al., 2010; Strub et al., 1998). The PUC hampers the reach of more oxygenated subtropical waters (SAAW, AAIW), extending the low-oxygen ESSW along the South American continental slope (Llanillo et al., 2012; Shaffer et al., 1995; Silva et al., 2009; Silva & Neshyba, 1979). A fraction of the low-oxygen waters carried by the PUC upwells at different locations along the continental slope (Strub et al., 1998). Part of these upwelled-waters can return equatorward with the PCC, parallel to the continental slope, and northwestward with the South Equatorial Current (SEC), subducting into the thermocline along the northern limb of the subtropical gyre, whereas another part drifts poleward as the wind-induced surface branch of the Subtropical Cell (STC) (Schott et al., 2004). The PCC transports well-oxygenated SAAW into the ESP-OMZ upper levels, which progressively mixes with the low-oxygen ESSW (Llanillo et al., 2013; Silva et al., 2009); Figure 4a illustrates the PCC along $\gamma_n =$ 26.56 kg m^{-3}, entering the ESP-OMZ between 81°W and 73°W.

At depths greater than 160 m and down to the OMZ's core ($\gamma_n =$ 26.81 kg m^{-3}, $z \cong$ 350 m), the average dianeutral velocity (entrainment) changes sign and promotes downwelling instead of upwelling (Figure 3). A similar but deeper (300 m) inversion of the vertical velocity is found in the NA-OMZ (Peña-Izquierdo et al., 2015). In these layers, mean currents are weaker than above and the volume enclosed by the ESP-OMZ becomes larger than in overlying layers, as it spreads to the west and to the south with depth (Figures 1a and 1b). The PCC appears further offshore of the PUC, between 81°W and 76°W, reaching down to at least 700 m along 14°S (Figure 5b).

Deeper than 455 m ($\gamma_n =$ 27.0 kg m^{-3}), the mean advective flow is weaker than in the layers above (Figures 4c, 5a, and 5b). Here most AAIW flows northwestward within the subtropical gyre (Shaffer et al., 2004) and part of it may eventually return eastward with the PIC. The AAIW carried with the PIC, although aged and partially eroded, may contribute to ventilate the lower part of the ESP-OMZ. The turning of these interior waters shows up in the potential vorticity contours, which are zonally oriented along 12°S and get no longer diverted in the vicinity of the Chilean slope (Figure 6c). Some AAIW also flows equatorward taking a more direct route within the lower reaches of the PCC (Silva et al., 2009), playing an important role in the ventilation of the ESP-OMZ (Llanillo et al., 2013).

5. Ventilation of the ESP-OMZ

In this section, we first quantify the gross and net advective oxygen supply by the mean currents ventilating the ESP-OMZ, which is followed by the computation of all advective and diffusive oxygen transfers (both isoneutral and dianeutral) across the ESP-OMZ boundary.

5.1. Advective Oxygen Transport into the ESP-OMZ by Mean Currents

We are interested in the oxygen transport (kmol s^{-1}) associated with specific mean currents that ventilate the ESP-OMZ, i.e., the amount of dissolved oxygen carried by some coherent current that enters this OMZ. This oxygen input does not necessarily remain inside the ESP-OMZ as some may leave through

recirculations. Hence, we compute the oxygen transport of an individual current as the oxygen provided the first time it crosses the OMZ boundary (except for the 4°S boundary). We complement our description of each specific current by informing about its pathway of origin (subtropical versus tropical-equatorial), volumetric transport, and characteristic depth range (Table 1).

Several studies have suggested that the mean circulation ventilates the ESP-OMZ mainly through the eastward equatorial current system (Czeschel et al., 2011, 2015; Montes et al., 2014; Stramma et al., 2010a). Indeed, our results for the ESP-OMZ upper layers show that the tropical-equatorial pathway dominates the oxygen input with a total of 469.1 kmol s^{-1} (77.5% of the total isoneutral advective transport). The SSCC contributes with 118.1 kmol s^{-1} while the equatorial inflow crossing 4°S provides an oxygen transport of 253.8 kmol s^{-1}. The remaining oxygen transported by the tropical-equatorial pathway into the OMZ (97.2 kmol s^{-1}) is explained by eastward zonal flows south of 7°S. In these upper layers, however, our results also show a significant subtropical advective transport of oxygen (136.0 kmol s^{-1}, or 22.5% of the total) associated with the PCC (72.4 kmol s^{-1}) and the STG (63.6 kmol s^{-1}) (Table 1).

At the ESP-OMZ core layer, the tropical-equatorial advective oxygen transport (43.8 kmol s^{-1}) is dominated by the flow across the 4°S boundary (29.7 kmol s^{-1}), whereas the SSCC provides 3.8 kmol s^{-1} and the rest (10.3 kmol s^{-1}) is due to southward recirculations of the SSCC (Figure 4b and Table 1). In this core layer, the subtropical advective pathway peaks (30.6 kmol s^{-1}, or 41.1% of the total advective transport) with the STG providing 21.1 kmol s^{-1} while the PCC supplies 9.5 kmol s^{-1} of oxygen (Table 1 and supporting information Figures S4b and S6).

In the lower ESP-OMZ layers, we find that almost all the advective oxygen transport (435.7 kmol s^{-1}, or 94.0%) into the OMZ comes from the tropical-equatorial region (Table 1), as expected by the poleward migration of the subtropical gyre with depth (Reid, 1997). Here the PIC contributes with 86.4 kmol s^{-1} while the dSSCC provides 153.3 kmol s^{-1}, and the flow entering through the 4°S boundary leaks from the westward SEIC transporting 122 kmol s^{-1}. The rest of the tropical-equatorial inflow (74.0 kmol s^{-1}) belongs to a southward recirculation of the PIC (Figure 4c). In these deep layers, the weak subtropical advective pathway (27.8 kmol s^{-1}, or 6.0%) is dominated by the STG (18.1 kmol s^{-1}), with a weaker PCC contribution (9.7 kmol s^{-1}) (Table 1).

5.2. Net Oxygen Supply Through Advection and Diffusion

We turn now to all physical processes, including and beyond the mean currents discussed above, involved in the net ventilation of the ESP-OMZ layers, distinguishing their pathway of origin in the case of isoneutral processes. The net isoneutral oxygen supply (μmol kg^{-1} yr^{-1}) due to each process is obtained integrating separately the isoneutral advective and diffusive oxygen transports over the ESP-OMZ boundary corresponding to each pathway (subtropical versus equatorial-tropical). Similarly, the net dianeutral oxygen supply is computed integrating separately the dianeutral diffusive and advective oxygen transports over the upper and lower limits of each isoneutral layer considered within the ESP-OMZ.

In the upper layers, both isoneutral advection and isoneutral diffusion contribute to an oxygen gain (10.72 μmol kg^{-1} yr^{-1}, Table 2). Isoneutral advection provides the largest net oxygen gain with 6.46 μmol kg^{-1} yr^{-1} (60.3% in these layers) (Figures 7 and 8, and Table 2). This is due to a large contribution from the tropical-equatorial currents (5.54 μmol kg^{-1} yr^{-1}, 51.7%) whereas the subtropical currents only provide a net oxygen supply of 0.92 μmol kg^{-1} yr^{-1} (8.6%). In these layers, isoneutral diffusion is responsible for 4.26 μmol kg^{-1} yr^{-1} (39.8%) of the net oxygen supply, with tropical-equatorial and subtropical diffusion supplying equal amounts (each with 2.13 μmol kg^{-1} yr^{-1}, 19.9%). Thus, the tropical-equatorial advective pathway dominates net oxygen supply to the upper layers, mainly above $\gamma_n = 26.69$ kg m^{-3} ($z \cong 300$ m) (Figures 7a and 7b).

Dianeutral processes in the upper layers, in contrast, lead to oxygen loss (−4.21 μmol kg^{-1} yr^{-1}, Table 2). These layers gain volume (3.91 Sv) because of the convergence of isoneutral advection (Table 2), which is lost through dianeutral advection (entrainment) either upward toward the surface Ekman layer or downward to about 460 m, with the change in flow direction occurring at about $\gamma_n = 26.40$ kg m^{-3} ($z \cong 160$ m) (Figure 3). This entrainment accounts for most of the oxygen loss (−4.06 μmol kg^{-1} yr^{-1}) in the upper layers, but oxygen is also lost due to dianeutral diffusion toward the core layer (−0.15 μmol kg^{-1} yr^{-1}) (Table 2).

In the core layer, the weakening of the mean currents associated to the STC leads to reduced ventilation and thus to the strengthening of the vertical and horizontal oxygen gradients, causing turbulent diffusion to become the main source responsible for net oxygen supply. Isoneutral advection and both isoneutral and dianeutral diffusion provide a net oxygen supply of 3.46 μmol kg^{-1} yr^{-1} (Table 2). Isoneutral diffusion

Table 2
Net Volume Transports (Sv), Net Oxygen Supply (μmol kg^{-1} yr^{-1}) and Percentages of the Net Oxygen Supply (Positive/Negative Values Represent Gain/Loss in the ESP-OMZ) in the Upper and Core Layers of the ESP-OMZ, Indicating the Process (i.e., Advection, Diffusion, and Respiration), and the Region of Origin (TE, Tropical-Equatorial and ST, Subtropical)

OMZ strata	Process		Net volume transport (Sv)	Net O_2 supply (μmol kg^{-1} yr^{-1})	% of net O_2 supply
Upper layers γ_n = 25.87 - 26.75 kg m^{-3} $z \cong$ 65 - 325 m V = 1.20 Pm^3	Isoneutral advection	TE	3.38	5.54 ± 0.43	51.7 ± 4.0
		ST	0.53	0.92 ± 0.07	8.6 ± 0.7
	Isoneutral diffusion	TE	-	2.13 ± 0.24	19.9 ± 2.2
		ST	-	2.13 ± 0.24	19.9 ± 2.2
	Dianeutral diffusion		-	-0.15 ± 0.03	-1.3 ± 0.3
	Dianeutral advection		-3.91	-4.06 ± 0.55	-37.9 ± 5.2
	aOUR		-	-6.51 ± 1.83	-60.8 ± 17.1
Core layers γ_n = 26.75 - 26.87 kg m^{-3} $z \cong$ 325 - 385 m V = 0.54 Pm^3	Isoneutral advection	TE	-0.10	0.00 ± 0.00	0.0
		ST	0.13	0.38 ± 0.03	11.0 ± 0.9
	Isoneutral diffusion	TE	-	0.45 ± 0.05	13.0 ± 1.4
		ST	-	2.03 ± 0.22	58.7 ± 6.5
	Dianeutral diffusion		-	0.60 ± 0.12	17.3 ± 3.5
	Dianeutral advection		-0.03	-0.16 ± 0.02	-4.6 ± 0.6
	aOUR		-	-3.30 ± 0.93	-95.4 ± 25.8

Note. Errors are estimated at the 95% confidence interval. Note that each range of layers has a different volume and that the net O_2 supply values are normalized (per kg).

delivers the largest net oxygen supply (2.48 μmol kg^{-1} yr^{-1}, with 58.7% from the subtropics and 13.0% from the tropical-equatorial region), followed by dianeutral diffusion with 0.60 μmol kg^{-1} yr^{-1} (17.3%). Subtropical isoneutral advection only inputs 0.38 μmol kg^{-1} yr^{-1} (11.0%) and the tropical-equatorial advective pathway is negligible at this layer. Thus, considering both diffusive and advective oxygen fluxes, the subtropical pathway is the dominant supplier of oxygen in this core layer (Table 2, Figures 7 and 8, and supporting information Figure S6), and the only physical process behind oxygen loss is dianeutral entrainment (−0.16 μmol kg^{-1} yr^{-1}) (Table 2).

Considering the deep layers of the ESP-OMZ, oxygen is supplied (1.55 μmol kg^{-1} yr^{-1}) only by isoneutral diffusion, with 71.0% from the tropical-equatorial region and 29.0% from the subtropics (Figures 7 and 8 and Table 3). The low-oxygen gain by subtropical diffusion in the deep layers is related to the poleward migration of the minimum geopotential anomaly, which separates the tropical and subtropical pathways. In these deep layers, oxygen is physically lost (−0.38 μmol kg^{-1} yr^{-1}) by isoneutral advection (−0.14 μmol kg^{-1} yr^{-1}, split equally between the subtropical and equatorial-tropical pathways) and also by downward entrainment (−0.23 μmol kg^{-1} yr^{-1}), and by weak dianeutral diffusion (−0.01 μmol kg^{-1} yr^{-1}) (Table 3 and Figures 1b and 3).

5.3. Biological Utilization

Recent studies have found that the ESP-OMZ is among those regions with the weakest oxygen trends in the entire ocean (Ito et al., 2017; Schmidtko et al., 2017), much less than 0.1 μmol yr^{-1} at 400 m (Ito et al., 2017). Assuming that the ESP-OMZ is in steady state, the net oxygen supply should be compensated by biological consumption. Therefore, we can estimate the mean biological consumption necessary to close the oxygen budget for each layer as well as for the entire ESP-OMZ volume (Tables 2 and 3, Figures 8a, 8b, and 9). The resulting

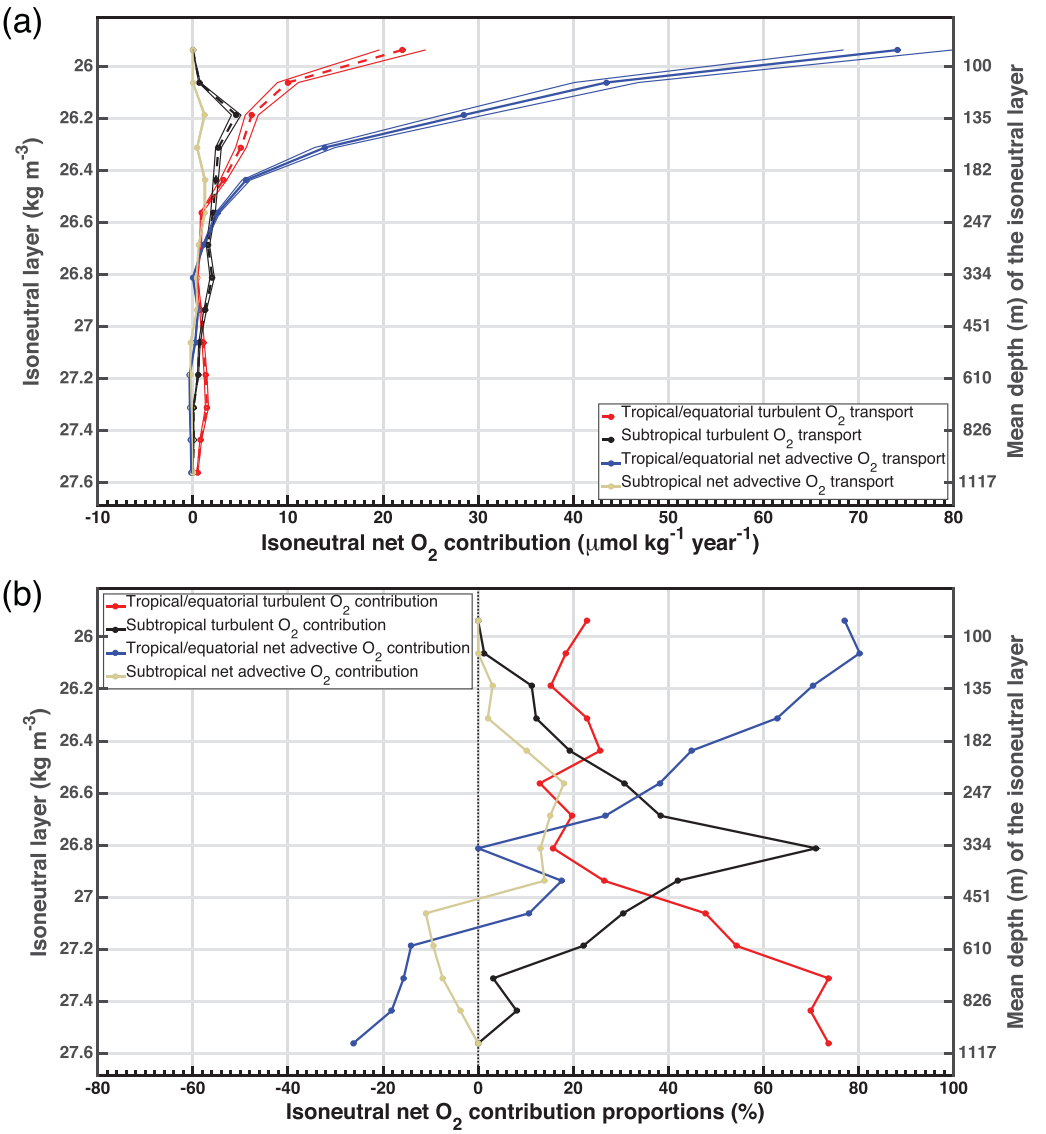

Figure 7. (a) Isoneutral net oxygen contributions to the ESP-OMZ (μmol kg^{-1} yr^{-1}) due to advection and turbulent diffusion. The thin lines represent the 95% confidence interval for each term after an error propagation analysis. Note that the values are normalized per kg. (b) Same as before but showing the relative contribution of each term in each layer.

vertical distribution gives negative *aOUR* at depths between 70 and 110 m depth (oxygen production) and positive rates (oxygen consumption) elsewhere, with peak values in the upper layers of the ESP-OMZ (Figure 9).

We validate our estimate of *aOUR* (Figure 9) with three independent evaluations: (1) using the vertical velocity from the assimilative ocean model SODA 2.2.4 to close the oxygen budget inside each layer (Carton & Giese, 2008); (2) using Karstensen et al.'s (2008) empirical expression, calculated using the apparent oxygen utilization (difference between the in situ oxygen and the saturation value at formation) and tracer-based water ages, for depths greater than 100 m over the entire Pacific Ocean; and (3) using the *aOUR* values obtained from net community production (NCP) values immediately below the seasonal thermocline (Czeschel et al., 2015), with an O_2:C Redfield ratio of 150:106 (Anderson, 1995).

Our estimate of *aOUR* fits remarkably well within the 95% confidence interval values provided by Karstensen et al. (2008) and generally follows the SODA-derived *aOUR*. The oxygen production from 70 to 100 m is consistent with biological activity between winter convective events and fits well, within the 95% confidence interval, the *aOUR* values in Czeschel et al. (2015).

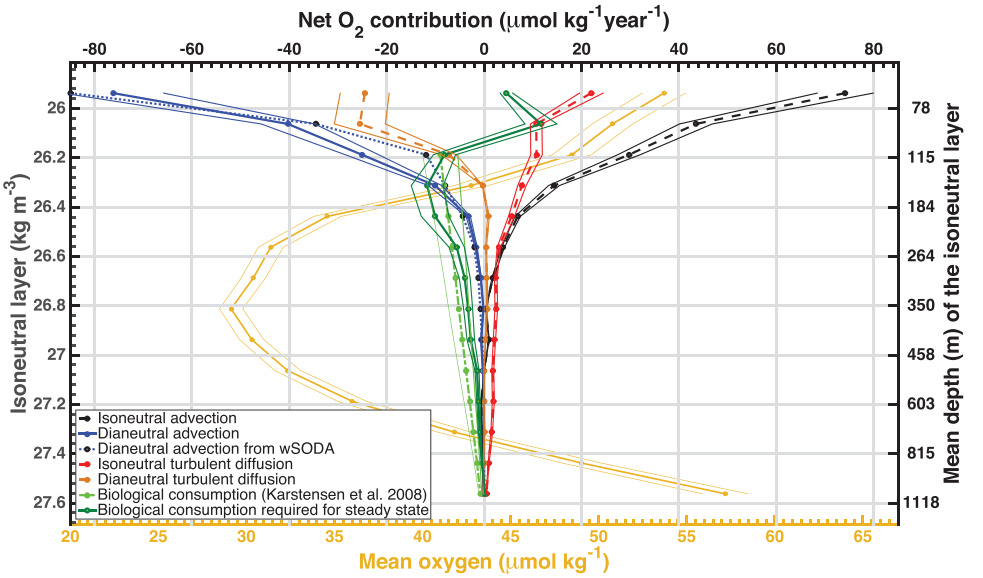

Figure 8. Terms involved in the annual-mean oxygen budget (μmol kg^{-1} yr^{-1}) for each isoneutral layer inside the ESP-OMZ, including the dianeutral advection (entrainment, solid blue line) and diffusion (orange line). For comparison, we show the contributions of dianeutral advection estimated using SODA's vertical velocity (dotted blue line) and the biological consumption as inferred from Karstensen et al. (2008) (light green line). Note that the values are normalized per kg. The mean oxygen profile (μmol kg^{-1}) within the ESP-OMZ is also shown (yellow line with points at the center of the isoneutral layers). The thin lines represent the 95% confidence interval for each term after an error propagation analysis.

Table 3
Same as in Table 2 but for the Lower Layers and for the Entire ESP-OMZ Volume

OMZ strata	Process		Net volume transport (Sv)	Net O_2 supply (μmol kg^{-1} yr^{-1})	% of net O_2 supply
Lower layers γ_n = 26.87 - 27.62 kg m^{-3} $z \cong$ 385 - 1160 m V = 4.22 Pm^3	Isoneutral advection	TE	-0.51	-0.07 ± 0.01	-4.5 ± 0.3
		ST	-0.18	-0.07 ± 0.01	-4.5 ± 0.3
	Isoneutral diffusion	TE	-	1.10 ± 0.12	71.0 ± 7.8
		ST	-	0.45 ± 0.05	29.0 ± 3.2
	Dianeutral diffusion		-	-0.01 ± 0.00	-0.7 ± 0.1
	Dianeutral advection		0.69	-0.23 ± 0.03	-14.8 ± 2.0
	aOUR		-	-1.17 ± 0.33	-75.5 ± 21.2
OMZ entire volume γ_n = 25.87 - 27.62 kg m^{-3} $z \cong$ 65 - 1160 m V = 5.96 Pm^3	Isoneutral advection	TE	2.77	1.06 ± 0.08	27.6 ± 2.1
		ST	0.47	0.17 ± 0.01	4.4 ± 0.3
	Isoneutral diffusion	TE	-	1.24 ± 0.14	32.3 ± 3.6
		ST	-	0.93 ± 0.10	24.2 ± 2.7
	Dianeutral diffusion		-	0.44 ± 0.09	11.5 ± 2.4
	Dianeutral advection		-3.24	-0.99 ± 0.13	-25.8 ± 3.5
	aOUR		-	-2.85 ± 0.80	-74.2 ± 20.8

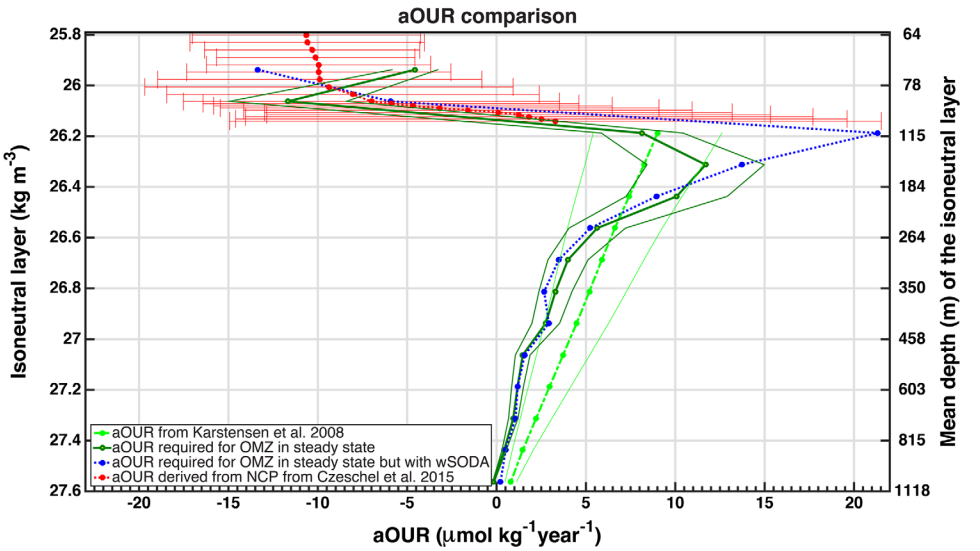

Figure 9. Apparent oxygen utilization rate *aOUR* (dark green line, μmol kg^{-1} yr^{-1}) necessary to close the oxygen budget inside the ESP-OMZ (assuming steady state). These values are compared with three independent *aOUR* estimates: (1) as obtained using the vertical velocity *w* from the assimilative ocean model SODA 2.2.4 (blue line), (2) as obtained from Karstensen et al.'s (2008) empirical expression for waters below 100 m for the entire Pacific Ocean (light green line), and (3) as deduced from Czeschel et al.'s (2015) oxygen float measurements below the seasonal thermocline (red dots). The thin lines and error bars represent the errors estimated with a 95% confidence interval.

The normalized consumption curves (independent of layer volume) show clear differences between the upper and lower layers, with oxygen consumption decreasing with depth (Figure 9). This is explained by the colder water temperatures with increasing depth; in fact, 95% of ocean oxygen consumption is driven by temperature rather than depth (Brewer & Peltzer, 2017). The good comparison of *aOUR* with several independent estimates thus validates our methodology to compute turbulent and advective oxygen fluxes (from which the biological term is derived).

5.4. Annual-Mean Oxygen Budget for the ESP-OMZ

Considering our entire ESP-OMZ volume, the annual-mean net oxygen budget is as follows: tropical-equatorial isoneutral turbulent diffusion dominates with 1.24 ± 0.14 μmol kg^{-1} yr^{-1} (32.3%), followed by tropical-equatorial advection with 1.06 ± 0.08 μmol kg^{-1} yr^{-1} (27.6%), subtropical isoneutral diffusion with 0.93 ± 0.10 μmol kg^{-1} yr^{-1} (24.2%), dianeutral diffusion with 0.44 ± 0.09 μmol kg^{-1} yr^{-1} (11.5%), and subtropical advection with 0.17 ± 0.01 μmol kg^{-1} yr^{-1} (4.4%). Dianeutral entrainment acts as an oxygen sink of -0.99 ± 0.13 μmol kg^{-1} yr^{-1} (25.8% of the net oxygen supply), largely explained by the upwelling into the surface layer. Finally, assuming steady state, the biological consumption required to close the oxygen budget is -2.85 ± 0.80 μmol kg^{-1} yr^{-1} (74.2% of the net oxygen supply) (Table 3), in good agreement with the value obtained (-3.71 ± 1.48 μmol kg^{-1} yr^{-1}) when using the empirical expression provided by Karstensen et al. (2008).

6. Concluding Remarks

We have provided a complete picture of the physical processes involved in the ventilation of the ESP-OMZ throughout its different layers, both in terms of the process (advection versus diffusion) and the origin of the oxygen supply (tropical-equatorial or subtropical). Oxygen supply by several mean currents has also been quantified and a refined annual-mean oxygen budget has been derived for the ESP-OMZ under the assumption of steady state.

Our results are conditioned by our definition of the ESP-OMZ, as the volume delimited by the 60 μmol kg^{-1} oxygen isosurface together with an artificial northern boundary along 4°S. Since the control volume is constant, the volume transport into or out of the entire ESP-OMZ must be nondivergent; hence, the selection of a constant-oxygen boundary would cause the net advective oxygen transport to be zero. This is not

quite the case because of our choice of the OMZ northern boundary along a parallel (where oxygen concentration is not constant), yet it is a fairly good first-order approximation for the overall ESP-OMZ. Nevertheless, the situation changes if we split the control volume in two regions: the net advective oxygen transport does not have to be zero for each of them. This is precisely what we have done when dividing the boundary of the ESP-OMZ into one subtropical pathway and one equatorial-tropical pathway. Additionally, our analysis shows that the isoneutral volume transport for each individual layer is divergent, so indeed the isoneutral volume and oxygen transports into each layer are nonzero. This translates into dianeutral velocities—unidirectional transfer of mass and oxygen between adjacent layers—which we have interpreted as dianeutral advection (entrainment).

In the first part of this study, we have quantified the oxygen transported by mean currents into the ESP-OMZ, distinguishing between their pathways of origin: tropical-equatorial versus subtropical. The tropical-equatorial advective pathway is composed of zonal currents flowing eastward into the ESP-OMZ plus the mean flow crossing the boundary at 4°S. Within this pathway, we highlight the Southern Subsurface Countercurrent (SSCC), its deep branch (dSSCC), and the poorly examined Polynesian Intermediate Current (PIC). The PIC has not been considered in previous OMZ ventilation studies although it contributes 19.8% of the tropical-equatorial advective oxygen transport (435.7 kmol s^{-1}) between 26.87 and 27.50 kg m^{-3}. The subtropical pathway is composed of both the northwestward flow of the subtropical gyre (STG) and the Peru-Chile Current (PCC). The subtropical advective oxygen transported into the OMZ is weak, as expected for a shadow zone; however, it is not negligible at the core layer of the ESP-OMZ where it peaks with 41.1% of the total advective oxygen transport (74.4 kmol s^{-1}), hence providing a non-negligible net oxygen supply (0.38 μmol kg^{-1} yr^{-1}) that contrasts with the null tropical-equatorial net oxygen advective supply.

In the second part of this study, we have compared the physical processes involved in the ventilation of the ESP-OMZ at different layers, considering its geographic origin and relative contribution to the annual-mean oxygen budget. Oxygen trends are very weakly decreasing in the region of the ESP-OMZ (Ito et al., 2017; Schmidtko et al., 2017), so we can reasonably assume that the ESP-OMZ is in steady state, allowing the biological respiration to be estimated as the residual. Note that we have only estimated the climatological biological consumption, whereas the microbial oxygen consumption is expected to increase in a warming ocean, further contributing to ocean deoxygenation (Brewer & Peltzer, 2017).

In the upper layers, advection clearly dominates net oxygen supply over turbulent diffusion by means of a high tropical-equatorial advection. Here almost half of the net oxygen supply escapes through dianeutral oxygen fluxes, part of it through Ekman pumping into the surface mixed layer as part of the STC dynamics. Consequently, one-way dianeutral velocities (entrainment related to upwelling in the top 160 m) arise as a relevant oxygen sink linked to the state of the STC. Changes in the intensity of the STC, mediated by shifts in the large-scale wind stress curl, may therefore alter the oxygen balance within this OMZ, as recently suggested for the observed decadal change in the NA-OMZ (Hahn et al., 2017). In the core and lower layers, the circulation associated with the STC weakens and turbulent diffusion dominates oxygen supply. Combining isoneutral and dianeutral fluxes, turbulent (two-way exchange) diffusion is responsible for two-thirds of the overall net oxygen supply into the ESP-OMZ, whereas advection contributes with one-third.

Regarding the pathway of origin, almost two-thirds of the total net oxygen supply (considering both advection and turbulent diffusion) to the ESP-OMZ takes place from the tropical/equatorial region, where almost half of this supply occurs via advection (traditional advective route). The previously unrecognized subtropical pathway contributes about one-quarter of the ventilation, mainly via turbulent diffusion. Furthermore, the subtropical pathway provides ∼70% of the net oxygen supply at the core layer of this OMZ. For comparison, Peña-Izquierdo et al. (2015) found that half of the water mass in the North Atlantic (NA) OMZ core has a subtropical origin, which suggests a relevant subtropical oxygen supply also in the NA-OMZ. Finally, dianeutral diffusive exchange plays a less relevant though non-negligible role in the ventilation of the ESP-OMZ, whereas dianeutral entrainment accounts for one-quarter of the total oxygen sink, the rest being lost by biological consumption (assuming steady state).

The uncertainty in the isoneutral diffusion coefficient is an important issue, as it sets the intensity of the isoneutral diffusive flux of oxygen into the ESP-OMZ. In numerical models, the selection of a proper diffusion value is often a laborious task, requiring a careful empirical tuning; in particular, as the mixing-length hypothesis tells us that diffusion is directly proportional to the horizontal size of the turbulent eddies, we may expect the isoneutral

diffusion coefficient to depend on the model's grid size. Here, we have used Chaigneau and Pizarro (2005) isoneutral diffusion estimates for the ESP-OMZ, obtained from correlations between velocity variations, as deduced using Lagrangian trajectories over grid elements of 2° of latitude-longitude. This methodology removes the coefficient dependence on grid size and relies on the velocity fields being highly correlated for scales up to about 200 km, a condition plenty fulfilled in the equatorial Pacific (Fujii & Kamachi, 2003).

Gnanadesikan et al. (2013) followed a very different, nearly opposite, approach to study the world's hypoxic regions. They estimated the *aOUR* from satellite data and used the residual of the oxygen budget to obtain horizontal eddy diffusivity coefficients of order 1,000 $m^2\ s^{-1}$. These values are of the same order of magnitude but substantially different from Chaigneau and Pizarro's (2005) diffusion coefficients (2,300 and 4,800 $m^2\ s^{-1}$ for the meridional and zonal coefficients). This comparison sustains the idea that we have accomplished a first-order description of the mean diffusive transports, but also warns us that there remains work to be done in order to obtain more accurate estimates.

Finally, we may hypothesize what would happen if we carried out a similar oxygen-budget analysis for a smaller volume, enclosed by a lower oxygen concentration contour such as the 19.5 $\mu mol\ kg^{-1}$ isosurface (Figure 1). The velocity fields (Figures 4 and 5) and advective oxygen fluxes (Figure 2) indeed allow us to anticipate that the fluxes into this inner region are less intense, as expected from the very low-oxygen concentrations, with a decreasing influence from the subtropical gyre and relatively larger ventilation from the tropical/equatorial region. We may also wonder what would be the relative influence of diffusion and advection on this smaller volume. While the area with oxygen concentration less than 19.5 $\mu mol\ kg^{-1}$ is located in a zone of sluggish circulation, the horizontal oxygen gradients are also very weak, leading to weaker isoneutral diffusive transports. Hence, both the diffusive and advective fluxes will decrease but we have no way to predict how their relative contributions will change.

Using climatological annual-mean data has the advantage of greatly increasing the amount of available data, but ignores changes at seasonal, interannual, and interdecadal scales. In particular, we have ignored any variability related to El Niño-Southern-Oscillation (ENSO), which induces substantial changes in the oceanographic conditions of the ESP-OMZ upper layers (e.g., Barber & Chavez, 1983; Llanillo et al., 2013; Philander, 1983), as well as shifts associated with the Pacific Decadal Oscillation (PDO), which reach deeper in the water column (Chavez et al., 2003; Deutsch et al., 2011; Mantua et al., 1997). Nevertheless, the description of the annual-mean oxygen pathways and budget represents a fundamental step forward in our understanding of the ESP-OMZ.

Acknowledgments
P.J. Llanillo acknowledges support from CONICYT/FONDECYT through the Postdoctorado project 3150229. J.L. Pelegrí and J. Peña-Izquierdo acknowledge funding by the Spanish Ministerio de Economía y Competitividad through projects TIC-MOC (CTM2011-28867) and VA-DE-RETRO (CTM2014-56987-P). R.R. Cordero gratefully acknowledges support from INACH (Preis RT_32-15), CONICYT-ANILLO (Preis ACT1410), FONDECYT (Preis 1151034), USACH-Basal USA 155, CORFO (Preis 16BPE2-66227) and USACH (Preis USA1555). Rena Czeschel and Lothar Stramma generously provided the float 3900727 NCP data set and useful comments. Dean Roemmich and John Gilson provided the Argo-derived climatological fields of salinity and temperature (http://sio-argo.ucsd.edu/RG_Climatology.html). John Gilson, Trevor McDougall, Paul Barker, and Nathalie Zilberman provided useful clarifications. The authors acknowledge the data sets made freely available by NODC (http://www.nodc.noaa.gov/OC5/woa13/), the Argo Program (http://www.argo.ucsd.edu), the ECMWF (http://www.ecmwf.int/en/research/climate-reanalysis/era-interim), and the APDRC (http://apdrc.soest.hawaii.edu/datadoc/soda_2.2.4.php).

References

Anderson, L. A. (1995). On the hydrogen and oxygen content of marine phytoplankton. *Deep-Sea Research Part I*, *42*, 1675–1680.
Barber, R. T., & Chavez, F. P. (1983). Biological consequences of El Niño. *Science*, *222*(4629), 1203–1210.
Brandt, P., Banyte, D., Dengler, M., Didwischus, S.-H., Fischer, T., Greatbatch, R. J., et al. (2015). On the role of circulation and mixing in the ventilation of oxygen minimum zones with a focus on the eastern tropical North Atlantic. *Biogeosciences*, *11*(12), 489–512. https://doi.org/10.5194/bgd-11-12069-2014
Brewer, P. G., & Peltzer, E. T. (2017). Depth perception: The need to report ocean biogeochemical rates as functions of temperature, not depth. *Philosophical Transactions of the Royal Society A*, *375*(2102). https://doi.org/10.1098/rsta.2016.0319
Carton, J. A., & Giese, B. S. (2008). A reanalysis of ocean climate using simple ocean data assimilation (SODA). *Monthly Weather Review*, *136*(8), 2999–3017. https://doi.org/10.1175/2007MWR1978.1
Castellanos, P., Pelegrí, J. L., Campos, E. J. D., Rosell-Fieschi, M., & Gasser, M. (2015). Response of the surface tropical Atlantic Ocean to wind forcing. *Progress in Oceanography*, *134*, 271–292. https://doi.org/10.1016/j.pocean.2015.02.005
Chaigneau, A., & Pizarro, O. (2005). Mean surface circulation and mesoscale turbulent flow characteristics in the eastern South Pacific from satellite tracked drifters. *Journal of Geophysical Research: Oceans*, *110*, C05014. https://doi.org/10.1029/2004JC002628
Chavez, F. P., Ryan, J., Lluch-Cota, S. E., & Niquen, C. M. (2003). From anchovies to sardines and back: Multidecadal change in the Pacific Ocean. *Science*, *299*(5604), 217–221. https://doi.org/10.1126/science.1075880
Codispoti, L. A., Brandes, J. A., Christensen, J. P., Devol, A. H., Naqvi, S. W. A., Paerl, H. W., et al. (2001). The oceanic fixed nitrogen and nitrous oxide budgets: Moving targets as we enter the anthropocene? *Scientia Marina*, *65*(Suppl. 2), 85–105.
Csanady, G. T. (1989). Energy dissipation and upwelling in a western boundary current. *Journal of Physical Oceanography*, *19*(4), 462–473.
Czeschel, R., Stramma, L., & Johnson, G. C. (2012). Oxygen decreases and variability in the eastern equatorial Pacific. *Journal of Geophysical Research: Oceans*, *117*, C11019. https://doi.org/10.1029/2012JC008043
Czeschel, R., Stramma, L., Schwarzkopf, F. U., Giese, B. S., Funk, A., & Karstensen, J. (2011). Middepth circulation of the eastern tropical South Pacific and its link to the oxygen minimum zone. *Journal of Geophysical Research: Oceans*, *116*, C01015. https://doi.org/10.1029/2010JC006565
Czeschel, R., Stramma, L., Weller, R. A., & Fischer, T. (2015). Circulation, eddies, oxygen, and nutrient changes in the eastern tropical South Pacific Ocean. *Ocean Science*, *11*(3), 455–470. https://doi.org/10.5194/os-11-455-2015
Dee, D. P., Uppala, S. M., Simmons, A. J., Berrisford, P., Poli, P., Kobayashi, S., et al. (2011). The ERA-Interim reanalysis: Configuration and performance of the data assimilation system. *Quarterly Journal of the Royal Meteorological Society*, *137*(656), 553–597. https://doi.org/10.1002/qj.828
Deutsch, C., Brix, H., Ito, T., Frenzel, H., & Thompson, L. (2011). Climate-forced variability of ocean hypoxia. *Science*, *333*(6040), 336–339. https://doi.org/10.1126/science.1202422

Fiedler, P. C., & Talley, L. D. (2006). Hydrography of the eastern tropical Pacific: A review. *Progress in Oceanography*, *69*(2–4), 143–180. https://doi.org/10.1016/j.pocean.2006.03.008

Fischer, T., Banyte, D., Brandt, P., Dengler, M., Krahmann, G., Tanhua, T., et al. (2013). Diapycnal oxygen supply to the tropical North Atlantic oxygen minimum zone. *Biogeosciences*, *10*(7), 5079–5093. https://doi.org/10.5194/bg-10-5079-2013

Fuenzalida, R., Schneider, W., Garces-Vargas, J., Bravo, L., & Lange, C. (2009). Vertical and horizontal extension of the oxygen minimum zone in the eastern South Pacific Ocean. *Deep-Sea Research Part II*, *56*(16), 992–1003.

Fujii, Y., & Kamachi, M. (2003). Three-dimensional analysis of temperature and salinity in the equatorial Pacific using a variational method with vertical coupled temperature-salinity empirical orthogonal function modes. *Journal of Geophysical Research: Oceans*, *108*(C9), 3297. https://doi.org/10.1029/2002JC001745

Garcia, H. E., Locarnini, R. A., Boyer, T. P., Antonov, J. I., Baranova, O. K., Zweng, M. M., et al. (2014). World Ocean Atlas 2013 Volume 3: Dissolved oxygen, apparent oxygen utilization, and oxygen saturation. In S. Levitus (Ed.), *NOAA Atlas NESDIS 75* (344 pp.). Washington, DC: U.S. Government Printing Office.

Gnanadesikan, A., Bianchi, D., & Pradal, M.-A. (2013). Critical role for mesoscale eddy diffusion in supplying oxygen to hypoxic ocean waters. *Geophysical Research Letters*, *40*, 5194–5198. https://doi.org/10.1002/grl.50998

Gunther, E. R. (1936). *A report on oceanographical investigations in the Peru coastal current*. Cambridge, UK: Lewis at the Cambridge University Press.

Hahn, J., Brandt, P., Greatbatch, R. J., Krahmann, G., & Körtzinger, A. (2014). Oxygen variance and meridional oxygen supply in the Tropical North East Atlantic oxygen minimum zone. *Climate Dynamics*, *43*(11), 2999–3024. https://doi.org/10.1007/s00382-014-2065-0

Hahn, J., Brandt, P., Schmidtko, S., & Krahmann, G. (2017). Decadal oxygen change in the eastern tropical North Atlantic. *Ocean Science*, *1*, 1–43. https://doi.org/10.5194/os-2016-102

Helly, J. J., & Levin, L. A. (2004). Global distribution of naturally occurring marine hypoxia on continental margins. *Deep-Sea Research Part I*, *51*(9), 1159–1168. https://doi.org/10.1016/j.dsr.2004.03.009

Helm, K. P., Bindoff, N. L., & Church, J. A. (2011). Observed decreases in oxygen content of the global ocean. *Geophysical Research Letters*, *38*, L23602. https://doi.org/10.1029/2011GL049513

Hofmann, A. F., Peltzer, E. T., Walz, P. M., & Brewer, P. G. (2011). Hypoxia by degrees: Establishing definitions for a changing ocean. *Deep-Sea Research Part I*, *58*(12), 1212–1226. https://doi.org/10.1016/j.dsr.2011.09.004

Ito, T., Minobe, S., Long, M. C., & Deutsch, C. (2017). Upper Ocean O_2 trends: 1958–2015. *Geophysical Research Letters*, *44*, 4214–4223. https://doi.org/10.1002/2017GL073613

Jackett, D. R., & McDougall, T. J. (1997). A neutral density variable for the world's oceans. *Journal of Physical Oceanography*, *27*(2), 237–263. https://doi.org/10.1175/1520-0485(1997)027<0237:ANDVFT>2.0.CO;2

Kalvelage, T., Jensen, M. M., Contreras, S., Revsbech, N. P., Lam, P., Günter, M., et al. (2011). Oxygen sensitivity of anammox and coupled N-cycle processes in oxygen minimum zones. *PLoS One*, *6*(12), e29299. https://doi.org/10.1371/journal.pone.0029299

Kalvelage, T., Lavik, G., Lam, P., Contreras, S., Arteaga, L., Löscher, C. R., et al. (2013). Nitrogen cycling driven by organic matter export in the South Pacific oxygen minimum zone. *Nature Geoscience*, *6*(3), 228–234. https://doi.org/10.1038/ngeo1739

Karstensen, J. (2004). Formation of the South Pacific shallow salinity minimum: A southern ocean pathway to the Tropical Pacific. *Journal of Physical Oceanography*, *34*(11), 2398–2412. https://doi.org/10.1175/jpo2634.1

Karstensen, J., Stramma, L., & Visbeck, M. (2008). Oxygen minimum zones in the eastern tropical Atlantic and Pacific oceans. *Progress in Oceanography*, *77*(4), 331–350. https://doi.org/10.1016/j.pocean.2007.05.009

Keeling, R. E., Körtzinger, A., & Gruber, N. (2010). Ocean deoxygenation in a warming world. *Annual Review of Marine Science*, *2*, 199–229. https://doi.org/10.1146/annurev.marine.010908.163855

Kessler, W. S. (2006). The circulation of the eastern tropical Pacific: A review. *Progress in Oceanography*, *69*(2–4), 181–217. https://doi.org/10.1016/j.pocean.2006.03.009

Llanillo, P. J., Karstensen, J., Pelegrí, J. L., & Stramma, L. (2013). Physical and biogeochemical forcing of oxygen and nitrate changes during El Niño/El Viejo and La Niña/La Vieja upper-ocean phases in the tropical eastern South Pacific along 86°W. *Biogeosciences*, *10*(10), 6339–6355. https://doi.org/10.5194/bg-10-6339-2013

Llanillo, P. J., Pelegrí, J., Duarte, C., Emelianov, M., Gasser, M., & Gourrion, J. (2012). Meridional and zonal changes in water properties along the continental slope off central and northern Chile. *Ciencias Marinas*, *38*, 307–332.

Luyten, J. R., Pedlosky, J., & Stommel, H. (1983). The ventilated thermocline. *Journal of Physical Oceanography*, *13*, 292–309. https://doi.org/10.1175/1520-0485(1983)013<0292:TVT>2.0.CO;2

Mantua, N. J., Hare, S. R., Zhang, Y., Wallace, J. M., & Francis, R. C. (1997). A Pacific interdecadal climate oscillation with impacts on Salmon production. *Bulletin of the American Meteorological Society*, *78*(6), 1069. https://doi.org/10.1175/1520-0477(1997)078<1069:apicow>2.0.co;2, 1997

Matear, R. J., & Hirst, A. C. (2003). Long-term changes in dissolved oxygen concentrations in the ocean caused by protracted global warming. *Global Biogeochemical Cycles*, *17*(4), 1125. https://doi.org/10.1029/2002GB001997

McDougall, T. J., & Klocker, A. (2010). An approximate geostrophic streamfunction for use in density surfaces. *Ocean Modelling*, *32*(3–4), 105–117. https://doi.org/10.1016/j.ocemod.2009.10.006

McDougall, T. J., & Barker, P. M. (2011). *Getting started with TEOS-10 and the Gibbs Seawater (GSW) Oceanographic Toolbox* (SCOR/IAPSO WG127, 28 pp.).

Montes, I., Colas, F., Capet, X., & Schneider, W. (2010). On the pathways of the equatorial subsurface currents in the eastern equatorial Pacific and their contributions to the Peru-Chile Undercurrent. *Journal of Geophysical Research: Oceans*, *115*, C09003. https://doi.org/10.1029/2009JC005710

Montes, I., Dewitte, B., Gutknecht, E., Paulmier, A., Dadou, I., Oschlies, A., et al. (2014). High-resolution modeling of the Eastern Tropical Pacific oxygen minimum zone: Sensitivity to the tropical oceanic circulation. *Journal of Geophysical Research: Ocean*, *119*, 5515–5532. https://doi.org/10.1002/2014JC009858

Morales, C. E., Hormazábal, S. E., & Blanco, J. (1999). Interannual variability in the mesoscale distribution of the depth of the upper boundary of the oxygen minimum layer off northern Chile (18–24S): Implications for the pelagic system and biogeochemical cycling. *Journal of Marine Research*, *57*(6), 909–932. https://doi.org/10.1357/002224099321514097

Nakano, H., & Suginohara, N. (2002). A series of middepth zonal flows in the Pacific driven by winds. *Journal of Physical Oceanography*, *32*(1997), 161–176. https://doi.org/10.1175/1520-0485(2002)032<0161:ASOMZF>2.0.CO;2

Oguz, T., Ducklow, H. W., & Malanotte-Rizzoli, P. (2000). Modeling distinct vertical biogeochemical structure of the Black Sea: Dynamical coupling of the oxic, suboxic, and anoxic layers. *Global Biogeochemical Cycles*, *14*(4), 1331–1352. https://doi.org/10.1029/1999GB001253

Paulmier, A., & Ruiz-Pino, D. (2009). Oxygen minimum zones (OMZs) in the modern ocean. *Progress in Oceanography*, *80*(3–4), 113–128. https://doi.org/10.1016/j.pocean.2008.08.001

Paulmier, A., Ruiz-Pino, D., Garçon, V., & Farías, L. (2006). Maintaining of the Eastern South Pacific oxygen minimum zone (OMZ) off Chile. *Geophysical Research Letters*, *33*, L20601. https://doi.org/10.1029/2006GL026801

Pelegrí, J., & Csanady, G. (1991). Nutrient transport and mixing in the Gulf Stream. *Journal of Geophysical Research: Oceans*, *96*(90), 2577–2583. https://doi.org/10.1029/90JC02535

Pelegrí, J. L., & Csanady, G. T. (1994). Diapycnal mixing in western boundary currents. *Journal of Geophysical Research: Oceans*, *99*(C9), 18275–18304. https://doi.org/10.1029/94JC01201

Peña-izquierdo, J., van Sebille, E., Pelegri, J. L., Sprintall, J., Mason, E., Llanillo, P. J., et al. (2015). Water mass pathways to the North Atlantic oxygen minimum zone. *Journal of Geophysical Research: Oceans*, *120*, 3350–3372, https://doi.org/10.1002/2014JC010557

Philander, S. G. H. (1983). El Nino Southern Oscillation phenomena. *Nature*, *302*(5906), 295–301.

Qiu, B., Rudnick, D. L., Chen, S., & Kashino, Y. (2013). Quasi-stationary North Equatorial Undercurrent jets across the tropical North Pacific Ocean. *Geophysical Research Letters*, *40*, 2183–2187. https://doi.org/10.1002/grl.50394

Reid, J. L. (1959). Evidence of a South Equatorial Countercurrent in the Pacific Ocean. *Nature*, *184*(4681), 209–210. https://doi.org/10.1038/184209a0

Reid, J. L. (1973). The shallow salinity minimum of the Pacific ocean. *Deep Sea Research and Oceanographic Abstracts*, *20*, 51–68.

Reid, J. L. (1997). On the total geostrophic circulation of the Pacific Ocean: Flow patterns, tracers, and transports. *Progress in Oceanography*, *39*(4), 263–352. https://doi.org/10.1016/S0079-6611(97)00012-8

Rowe, G., Firing, E., & Johnson, G. C. (2000). Pacific equatorial subsurface countercurrent velocity, transport, and potential vorticity*. *Journal of Physical Oceanography*, *30*, 1172–1187.

Sabine, C. L., Key, R. M., Kozyr, A., Feely, R. A., Wanninkhof, R., Millero, F. J., et al. (2005). *Global ocean data analysis project: Results and data* (ORNL/CDIAC-145, NDP-083). Oak Ridge, TN: Carbon Dioxide Information Analysis Center, Oak Ridge National Laboratory, U.S. Department of Energy. https://doi.org/10.3334/CDIAC/otg.ndp083

Schmidtko, S., Stramma, L., & Visbeck, M. (2017). Decline in global oceanic oxygen content during the past five decades. *Nature*, *542*(7641), 335–339. https://doi.org/10.1038/nature21399

Schmittner, A., Oschlies, A., Matthews, H. D., & Galbraith, E. D. (2008). Future changes in climate, ocean circulation, ecosystems, and biogeochemical cycling simulated for a business-as-usual CO_2 emission scenario until year 4000 AD. *Global Biogeochemical Cycles*, *22*, GB1013. https://doi.org/10.1029/2007GB002953

Schott, F. A., McCreary, J. P. Jr., & Johnson, G. C. (2004). Shallow overturning circulations of the tropical-subtropical oceans. In Wang, C., Xie, S. P., & Carton, J. A. (Eds.), *Earth's climate: The ocean-atmosphere interaction* (Vol. 147, pp. 261–230). Washington, DC: American Geophysical Union. https://doi.org/10.1029/147GM15

Shaffer, G., Hormazabal, S., Pizarro, O., & Ramos, M. (2004). Circulation and variability in the Chile Basin. *Deep-Sea Research Part I*, *51*(10), 1367–1386. https://doi.org/10.1016/j.dsr.2004.05.006

Shaffer, G., Salinas, S., Pizarro, O., Vega, A., & Hormazabal, S. (1995). Currents in the deep ocean off Chile (30°S). *Deep-Sea Research Part I*, *42*(4), 425–436. https://doi.org/10.1016/0967-0637(95)99823-6

Silva, N., & Neshyba, S. (1979). NOTE On the southernmost extension of the Peru-Chile Undercurrent. *Deep-Sea Research and Oceanographic Abstracts*, *26*(1971), 1387–1393.

Silva, N., Rojas, N., & Fedele, A. (2009). Water masses in the Humboldt Current System: Properties, distribution, and the nitrate deficit as a chemical water mass tracer for Equatorial Subsurface Water off Chile. *Deep-Sea Research Part II*, *56*(16), 1004–1020. https://doi.org/10.1016/j.dsr2.2008.12.013

Smethie, W. M. (1987). Nutrient regeneration and denitrification in low oxygen fjords. *Deep-Sea Research Part A*, *34*(5–6), 983–1006. https://doi.org/10.1016/0198-0149(87)90049-5

Stramma, L., Johnson, G. C., Firing, E., & Schmidtko, S. (2010a). Eastern Pacific oxygen minimum zones: Supply paths and multidecadal changes. *Journal of Geophysical Research: Oceans*, *115*, C09011. https://doi.org/10.1029/2009JC005976

Stramma, L., Johnson, G. C., Sprintall, J., & Mohrholz, V. (2008). Expanding oxygen-minimum zones in the tropical oceans. *Science*, *320*(5876), 655–658. https://doi.org/10.1126/science.1153847

Stramma, L., Schmidtko, S., Levin, L. A., & Johnson, G. C. (2010b). Ocean oxygen minima expansions and their biological impacts. *Deep-Sea Research Part I*, *57*(4), 587–595.

Stramma, L., Oschlies, A., & Schmidtko, S. (2012). Mismatch between observed and modeled trends in dissolved upper-ocean oxygen over the last 50 yr. *Biogeosciences*, *9*(10), 4045–4057. https://doi.org/10.5194/bg-9-4045-2012

Strub, P., Mesias, J., Montecino, V., Rutllant, J., & Salinas, S. (1998). Coastal ocean circulation off western South America. In Robinson, A. R., & Brink, K. H. (Eds.), *The sea: The global coastal ocean* (Vol. 11, pp. 272–313). New York, NY: Wiley.

Talley, L. D. (2007). In Sparrow, M., Chapman, P., & Gould, J. (Eds.), *Hydrographic Atlas of the World Ocean Circulation Experiment (WOCE) Volume 2: Pacific Ocean*. Southampton, UK: International WOCE Project Office. https://doi.org/10.21976/C6WC77

Talley, L. D., Pickard, G. L., Emery, W. J., & Swift, J. H. (2011). *Descriptive physical oceanography*. Amsterdam, Netherlands: Elsevier.

Tsuchiya, M. (1975). Subsurface Countercurrents in the eastern equatorial Pacific ocean. *Journal of Marine Research*, *33*(Suppl), 145–175.

Tsuchiya, M., & Talley, L. D (1996). Water-property distributions along an eastern Pacific hydrographic section at 135W. *Journal of Marine Research: Oceans*, *54*(3), 541–564.

Tsuchiya, M., & Talley, L. D. (1998). A Pacific hydrographic section at 88°W: Water-property distribution. *Journal of Geophysical Research: Oceans*, *103*(C6), 12899–12918. https://doi.org/10.1029/97JC03415

Turner, J. S. (1986). Turbulent entrainment: The development of the entrainment assumption, and its application to geophysical flows. *Journal of Fluid Mechanics*, *173*, 431–471. https://doi.org/10.1017/S0022112086001222

Ulloa, O., & Pantoja, S. (2009). The oxygen minimum zone of the eastern South Pacific. *Deep-Sea Research Part II*, *56*(16), 987–991. https://doi.org/10.1016/j.dsr2.2008.12.004

Whalen, C. B., Talley, L. D., & MacKinnon, J. A. (2012). Spatial and temporal variability of global ocean mixing inferred from Argo profiles. *Geophysical Research Letters*, *39*, L18612. https://doi.org/10.1029/2012GL053196

Wooster, W. S., & Gilmartin, M. (1961). The Peru-Chile Undercurrent. *Journal of Marine Research*, *19*, 97–122.

Zilberman, N. V., Roemmich, D. H., & Gille, S. T. (2013). The mean and the time variability of the shallow meridional overturning circulation in the tropical South Pacific Ocean. *Journal of Climate*, *26*(12), 4069–4087. https://doi.org/10.1175/JCLI-D-12-00120.1

Erratum

In the originally published version of this article, the affiliation for R.R. Cordero was incorrect. This error has since been corrected, and this version may be considered the authoritative version of record.